REPUBLIC OF TÜRKİYE

YILDIZ TECHNICAL UNIVERSITY

GRADUATE SCHOOL OF SCIENCE AND ENGINEERING

ASSESSMENT AND COMPARISON OF SPATIAL RESOLUTION IN HYBRID MEDICAL IMAGING MODALITIES UTILIZED IN NUCLEAR MEDICINE (PET/CT AND PET/MRI)

Burak KULA

MASTER OF SCIENCE THESIS

Department of Biomedical Engineering

Biomedical Engineering Program

Supervisor

Assoc. Prof. Dr. Osman GUNAY

July, 2024

REPUBLIC OF TÜRKİYE

YILDIZ TECHNICAL UNIVERSITY

GRADUATE SCHOOL OF SCIENCE AND ENGINEERING

ASSESSMENT AND COMPARISON OF SPATIAL RESOLUTION IN HYBRID MEDICAL IMAGING MODALITIES UTILIZED IN NUCLEAR MEDICINE (PET/CT AND PET/MRI)

A thesis submitted by Burak KULA in partial fulfilment of the requirements for the degree of MASTER OF SCIENCE was approved by the committee on 29.07.2024 in the Department of Biomedical Engineering, Biomedical Engineering Program.

Assoc. Prof. Dr. Osman GUNAY
Yıldız Technical University
Supervisor

Approved By the Examining Committee

Assoc. Prof. Dr. Osman GUNAY, Supervisor
Yildiz Technical University _____

Assoc. Prof. Dr. Ismail CANTURK, Member
Yildiz Technical University _____

Prof. Dr. Iskender AKKURT, Member
Suleyman Demirel University _____

I hereby declare that I have obtained the required legal permissions during data collection and exploitation procedures, that I have made the in-text citations and cited the references properly, that I haven't falsified and/or fabricated research data and results of the study and that I have abided by the principles of the scientific research and ethics during my Thesis Study under the title of "Assessment and Comparison of Spatial Resolution in hybrid medical imaging modalities utilized in nuclear medicine (PET/CT and PET/MRI)" supervised by my supervisor, Assoc. Prof. Dr. Osman GUNAY. In the case of a discovery of a false statement, I am to acknowledge any legal consequence.

Burak KULA

Signature

Dedicated…

…to healthcare practices

&

…to improving the quality of human life

ACKNOWLEDGEMENTS

I would like to express my sincere gratitude to Assoc. Prof. Dr. Osman GUNAY for his invaluable guidance, unwavering support, and profound insights throughout the entirety of this thesis project. His expertise, encouragement, and constructive feedback have been instrumental in shaping the direction and quality of my research.

I extend my heartfelt appreciation to Nami YEYIN and Mustafa DEMIR, for their insightful guidance, invaluable suggestions, and dedication to ensuring the completion of this work.

I am deeply thankful to Istanbul University Cerrahpasa Faculty of Medicine for providing the necessary resources, facilities, and opportunities that facilitated the completion of this thesis.

I extend my sincere appreciation to my manager, Nahal HOSSEINZADEH, and my employer, NOTICE d.o.o., for their unwavering patience, understanding, and support throughout my thesis journey and academic endeavours. Their flexibility and encouragement allowed me to balance the demands of work and school effectively, fostering an environment where I could pursue both professional growth and educational aspirations. Their willingness to accommodate my academic commitments and provide guidance whenever needed has been invaluable. I am grateful for the opportunities they have provided me, as well as the trust they have placed in my abilities, which have significantly contributed to my personal and professional development.

Special thanks are due to my family, Esma KARACA and Tuncer KULA, and my dear friend, Yeliz GULDORUM, for their unconditional love, encouragement, and understanding during the ups and downs of this endeavour. Their unwavering belief in my abilities has been a constant source of motivation and inspiration.

Lastly, I acknowledge the countless researchers, scholars, and practitioners whose work has laid the foundation for this thesis. Their contributions have enriched my understanding and fueled my passion for medical imaging.

Burak KULA

TABLE OF CONTENTS

TABLE OF CONTENTS v
LIST OF SYMBOLS vii
LIST OF ABBREVIATIONS viii
LIST OF FIGURES x
LIST OF TABLES xii
ABSTRACT xiii
ÖZET xv
1 INTRODUCTION 1
1.1 Radiation 1
1.1.1 Types of Radiation 2
1.1.2 Radioactive Isotopes and Radioactive Decay 4
1.2 Nuclear Medicine 12
1.2.1 Interactions of Radiation with Surrounding Matters 13
1.2.2 Radiopharmaceuticals in Nuclear Medicine 17
1.3 Therapeutic Applications of Nuclear Medicine 19
1.4 Diagnostic Applications of Nuclear Medicine 21
1.4.1 Anger Camera (Gamma Camera) and Single Photon Emission Computed Tomography (SPECT) 22
1.4.2 Positron Emission Tomography (PET) – PET/CT – PET/MRI 23
1.5 Spatial Resolution Assessment in PET/CT and PET/MRI 28
1.6 The Purpose of This Thesis 30
2 MATERIALS AND METHOD 31
2.1 Phantom Description 31
2.2 Experimental Setup 32
2.3 Data Analysis 35
3 RESULTS 37
3.1 Qualitative Assessment and Comparison 37
3.2 Quantitative Assessment and Comparison 38
4 DISCUSSION 41
5 CONCLUSION 43
REFERENCES 44
A APPENDIX MATERIALS AND METHOD 56
Appendix A.1 56

Appendix A.2 57
PUBLICATIONS FROM THE THESIS **59**

LIST OF SYMBOLS

E_{e^+}	Kinetic energy of the positron
E_e	Kinetic energy of the electron
E_B	Binding energy of the electron
E'_γ	Energy level of the scattered photon
E_γ	Energy level of the incident photon
$T_{1/2}$	Half-life
$\bar{\nu}$	Antineutrino
α	Alpha
β	Beta
γ	Gamma
λ	Radioactive decay constant
μCi	Microcurrie – a unit of radioactivity
Bq	Becquerel – a unit of radioactivity
c	Speed of light
cc	Cubic centimetre – a unit of volume
Ci	Curie – a of radioactivity
E	Energy level
eV	Electron volt
h	Plank constant
J	Joule – a unit of energy
keV	Kiloelectron volt
m	Mass
MBq	Mega becquerel – a unit of radioactivity
mCi	Millicurie – a unit of radioactivity
MeV	Mega electron volt
mm	Millimeter – the unit of length
s	Second – a unit of time
T	Tesla – a unit of magnetic field
t	time
ν	Neutrino

LIST OF ABBREVIATIONS

2D	Two dimensional
3D	Three dimensional
BGO	Bismuth germanate oxyorthosilicate
Br	Bromium
C	Carbon
csv	Comma-separated values
CT	Computed tomography
Cu	Copper
EC	Electron capture
EDTMP	Ethylene diamine tetramethylene phosphonic acid
F	Fluorine
FDG	Florodeoksiglukoz
FWHM	Full-width half maximum
Ga	Gallium
GSO	Gadolinium oxyorthosilicate
HCl	Hydrochloric acid
I	Iodine
In	Indium
IT	Isomeric transition
IV	Intravenous
KNC	Karlsruhe nuclide chart
LSO	Lutetium oxyorthosilicate
MIBG	Metaiodobenzylguanidine
MRI	Magnetic resonance imaging
N	Nitrogen
N/A	Not acceptable
NaI	Sodium iodine
NEMA	National Electrical Manufacturers Association
NHL	non-Hodgkin’s lymphoma
O	Oxygen
OSEM	Ordered subset expectation maximization
P	Phosphorus

PET	Positron emission tomography
PET/CT	Positron emission tomography/Computed tomography
PET/MRI	Positron emission tomography/Magnetic resonance imaging
PLA	Poly-lactic acid
PSF	Point spread function
PVNS	Pigmented villonodular synovitis
Ra	Radium
Rb	Rubidium
Re	Rhenium
RIT	Radioimmunotherapy
Sm	Samarium
Sn	Tin
SPECT	Single photon emission computed tomography
SPECT/CT	Single photon emission computed tomography/Computed tomography
Sr	Strontium
Tc	Technetium
Th	Thorium
Tl	Thallium
TOF	Time of flight
Y	Yttrium
Zr	Zirconium

LIST OF FIGURES

Figure 1.1 Periodic Table (Barry & Sadler, 2013). **1**

Figure 1.2 Electromagnetic Spectrum as Per Energy Levels (L'Annunziata, 2012). **2**

Figure 1.3 Non-Ionising and Ionising Radiation, and Their Exemplary Effects (Zamanian & Hardiman, 2005). **3**

Figure 1.4 Summary of Radiation Types (*Types of Radiation [MOE]*, n.d.). **4**

Figure 1.5 Karlsruhe Nuclide Chart 10th Edition, 2018 (Sóti et al., 2019). **5**

Figure 1.6 Illustration of Possible Decay Modes (Gibbons, 2019). **5**

Figure 1.7 Decay Notations of Alpha (A), Beta Minus (B), Beta Plus (C), Electron Capture (D) And Gamma (E) Decays (Bryan, 2023). **6**

Figure 1.8 Radioactive Decay Routes of Br-80 Isotope (Bryan, 2023). **6**

Figure 1.9 Decay Curve of Radioactive Atom A-32. Each Box Illustrates the Different Decay Steps, After One Half-Life (Powsner & Powsner, 2006). **7**

Figure 1.10 Conversion of Ci to Bq and MBq (Powsner & Powsner, 2006). **8**

Figure 1.11 General Representation of a Parent Atom Facing Alpha Decay (Washington & Leaver, 2015). **9**

Figure 1.12 Illustration of Beta Decay. (A) Beta-Minus Decay. (B) Beta-Plus Decay (Welsh, 2006). **10**

Figure 1.13 Illustration of Electron Capture. (A) Conversion Equation of Captured Electron to Neutron, (B) Illustration of Characteristic X-Ray Emission, (C) Illustration of Auger Effect (Martin & Godes, 2018). **11**

Figure 1.14 Illustration of Gamma Decay of an Excited Daughter Nucleus (Powsner & Powsner, 2006). **12**

Figure 1.15 The Two Possible Gamma Decay Processes of Excited Tc-99m Atom to Become Stable Tc-99 Atom (Powsner & Powsner, 2006). **12**

Figure 1.16 Illustration of The Photoelectric Effect (*Basic Physics of Nuclear Medicine/Interaction of Radiation with Matter - Wikibooks, Open Books for an Open World*, n.d.). **14**

Figure 1.17 Illustration of The Photoelectric Effect and Consecutive Events, Characteristic X-Ray and Auger Electron Emission (Rahman, 2017). **14**

Figure 1.18 Illustration of The Compton scattering (Qiao et al., 2021). **15**

Figure 1.19 Illustration of Pair Production (Chandra & Rahmin, 2018; Shaffer et al., 2016). **16**

Figure 1.20 Illustration of Annihilation of The Positron (Chandra & Rahmin, 2018). **17**

Figure 1.21 Illustration of Anger Camera (Powsner et al., 2013). **22**

Figure 1.22 Illustration of Rotating SPECT Cameras Around Patient (Bushberg, 2012). **23**

Figure 1.23 Illustration of Photon Detection in PET. (A) Illustration of Positron Annihilation, After Positron Decay of F-18 To O-18. (B) Photon Detection by The Corresponding Detector Pair in The Detector Ring of The PET Camera Including Representation of Line of Response and Tube of Response (Saturnino Guarino & Martelli, 2018). **24**

Figure 1.24 Configurations of Detectors in PET Systems. (A) Multiple Full Rings Configuration of Detector Blocks, Each Containing Discrete, Small-Area Detector Elements. (B) Multiple-Partial Ring Configuration of Detector Blocks, Each Composed of Small-Area Detector Elements. (C) Hexagonal Array Configuration of Detector Banks, With Each Bank Consisting of Small-Area Detector Elements. (D) Large-Area Detectors Configuration Which Placed as Opposed to Each Other, such as Anger Cameras. (E) Hexagonal Array Configuration of Detector Banks, with Each Bank Consisting of Large-Area Detector Elements. (F) Circular Configuration of Six Large-Area and Curved Detectors (Zanzonico, 2004). **25**

Figure 1.25 Illustrations of PET/MRI and PET/CT Hybrid Imaging Modalities. (A) PET/MRI modality (Kang & Yamaya, 2021). (B) PET/CT modality (Lameka et al., 2016). **26**

Figure 2.1 The Design Illustration of The Custom-Made PLA Phantom Used in This Thesis. (A) The Design of The Prism with Two Extensions. (B) The Illustration of Holes in The Mid-Section of The Prism's Frontal Surface and Their Strategic Separation. (C) The Design of Two Supports. (D) The Final Assembly of Custom-Made PLA Phantom. **32**

Figure 2.2 The Experimental Setup. **33**

Figure 2.3 Image Acquisition in PET/CT. **34**

Figure 3.1 The Radioactive Source Positions Loaded on The Phantom and The Corresponding Radioactivity Results. (A) Radioactive Source (FDG-18) Locations onto Phantom. (B) Radioactivity vs Distance (in mm) Graph for PET/CT, (C) Radioactivity vs Distance (in mm) Graph of PET/MRI. **38**

LIST OF TABLES

Table 1.1 Characteristics of Some Radionuclides Utilized in Therapeutic Nuclear Medicine (Yeong et al., 2014). **.....20**

Table 1.2 Common Radiopharmaceuticals in Therapeutic Nuclear Medicine (Yeong et al., 2014). **.....21**

Table 1.3 Advantages and Limitations of PET/CT (Ehman et al., 2017). **.....27**

Table 1.4 Advantages and Limitations of PET/MRI (Ehman et al., 2017). **.....27**

Table 3.1 FWHM Results for PET/CT. **.....39**

Table 3.2 FWHM Results for PET/MRI. **.....40**

ABSTRACT

Assessment and Comparison of Spatial Resolution in Hybrid Medical Imaging Modalities Utilized in Nuclear Medicine (PET/CT and PET/MRI)

Burak KULA

Department of Biomedical Engineering

Biomedical Engineering Program

Master of Science Thesis

Supervisor: Assoc. Prof. Dr. Osman GUNAY

Healthcare professionals' diagnostic abilities were improved by hybrid medical imaging modalities such as PET/CT and PET/MRI, which combined anatomical and functional data into a single image. Still, there are issues, particularly with spatial resolution, which is important for accurate disease identification.

A custom-made phantom with ten holes is designed using Solidworks and manufactured using additive manufacturing to assess the spatial resolution of PET/CT and PET/MRI. These holes were strategically positioned along the phantom's mid-line on the front surface. A plexiglass box was designed to enclose the phantom and filled water. The phantom was loaded with FDG-18. PET/CT and PET/MRI equipment were used for image acquisition, which were then processed using Image J and MATLAB to determine the full width at half maximum (FWHM) values.

The activity vs distance plots demonstrated that PET/CT was initially unable to distinguish the first five sources. Comparably, PET/MRI was unable to distinguish

the first four sources. Moreover, the examination of FWHM values for PET/CT showed that FWHM values up to the sixth source were unsatisfactory and FWHM for the remaining sources were acceptable. Additionally, a similar pattern was seen in PET/MRI, with relevant FWHM values starting from the sixth source. These were showing enhanced separation performance over certain ranges.

This study concludes by highlighting the unique strengths and weaknesses of PET/CT and PET/MRI in identifying radioactive sources in diagnostic nuclear medicine. The radioactivity vs distance plots clearly demonstrated the difficulties that both modalities had when they attempted to distinguish sources that were closely separated and demonstrated that PET/MRI's performance in this regard was superior to PET/CT's. However, at a certain distance, both molecular imaging methods performed well, as seen by significant FWHM values starting at the sixth source. These results underline how crucial it is to evaluate spatial resolution and differentiating ability as they have a direct bearing on how well complex biological structures may be diagnosed. The findings of this study will help to improve patient care by directing future developments in nuclear medicine and continuing to optimise imaging techniques.

Keywords: spatial resolution, distinguishing ability, activity against distance graph, full-width half-maximum (FWHM), PET/CT, PET/MRI.

ÖZET

Nükleer Tıpta Kullanılan Hibrit Tıbbi Görüntüleme Yöntemlerinde (PET/BT ve PET/MRI) Uzamsal Çözünürlüğün Değerlendirilmesi ve Karşılaştırılması

Burak KULA

Biyomedikal Muhendisligi Anabilim Dalı

Yüksek Lisan Tezi

Danışman: Assoc. Prof. Dr. Osman GUNAY

PET/BT ve PET/MRI gibi anatomik ve fonksiyonel verileri tek bir görüntüde birleştiren hibrit tıbbi görüntüleme yöntemleri sayesinde sağlık çalışanlarının teşhis yetenekleri geliştirilmiştir. Yine de, özellikle doğru hastalık tanımlaması için önemli olan uzaysal çözünürlükle ilgili sorunlar vardır.

PET/BT ve PET/MRI'nın uzaysal çözünürlüğünü değerlendirmek için Solidworks kullanılarak on delikli özel yapım bir fantom tasarlanmıştır ve 3 boyutlu yazıcı kullanılarak üretilmiştir. Bu delikler prizmanın ön yüzeyindeki orta hat boyunca stratejik olarak konumlandırıldı. Bir pleksiglas kutu yapıldı ve özel yapım fantomu 3D yazdırmak için PLA tozu kullanıldı. Fantom FDG-18 ile yüklendi. Görüntü elde etmek için PET/BT ve PET/MRI ekipmanı kullanıldı ve bunlar daha sonra Image J ve MATLAB kullanılarak işlenerek yarı maksimumda tam genişlik (FWHM) değerleri belirlendi.

Aktivite ve mesafe grafikleri PET/BT'nin başlangıçta ilk beş kaynağı ayırt edemediğini göstermiştir. Benzer şekilde, PET/MRI da ilk dört kaynağı ayırt

edememiştir. Ayrıca, PET/BT için FWHM değerlerinin incelenmesi, altıncı kaynağa kadar FWHM değerlerinin yetersiz olduğunu ve kalan kaynaklar için FWHM değerlerinin kabul edilebilir olduğunu göstermiştir. Ek olarak, PET/MRI'da da altıncı kaynaktan itibaren uygun FWHM değerleri ile benzer bir model görülmüştür. Bunlar belirli aralıklarda gelişmiş ayırma performansı gösteriyordu.

Bu çalışma, tanısal nükleer tıpta radyoaktif kaynakların belirlenmesinde PET/BT ve PET/MRI'ın benzersiz güçlü ve zayıf yönlerini vurgulayarak sonuçlanmaktadır. Radyoaktiviteye karşı mesafe grafikleri, her iki yöntemin de yakından ayrılmış kaynakları ayırt etmeye çalıştıklarında yaşadıkları zorlukları açıkça göstermiş ve PET/MRI'ın bu konudaki performansının PET/BT'den daha üstün olduğunu ortaya koymuştur. Bununla birlikte, belirli bir mesafede, altıncı kaynaktan itibaren önemli FWHM değerlerinde görüldüğü gibi, her iki moleküler görüntüleme yöntemi de iyi performans göstermiştir. Bu sonuçlar, karmaşık biyolojik yapıların ne kadar iyi teşhis edilebileceğini doğrudan etkilediğinden, uzaysal çözünürlük ve ayırt etme yeteneğinin değerlendirilmesinin ne kadar önemli olduğunun altını çizmektedir. Bu çalışmanın bulguları, nükleer tıpta gelecekteki gelişmeleri yönlendirerek ve görüntüleme tekniklerini optimize etmeye devam ederek hasta bakımının iyileştirilmesine yardımcı olacaktır.

Anahtar Kelimeler: uzamsal cozunurluk, ayristirma yetenegi, aktivite-mesafe grafigi, tam genislik yari yuksekligi (FWHM), PET/CT, PET/MRI.

1
INTRODUCTION

1.1 Radiation

All matter in nature comprises uncountable atoms which include nuclei and negative charges distributed in different shells around the nucleus. The nuclei determine the atom's identity due to the variety in the combination of the numbers of protons and neutrons in the nucleus. As a result of these various combinations, a total of 118 elements are named in nature, and placed on the periodic table based on their proton numbers as presented in Figure 1.1.

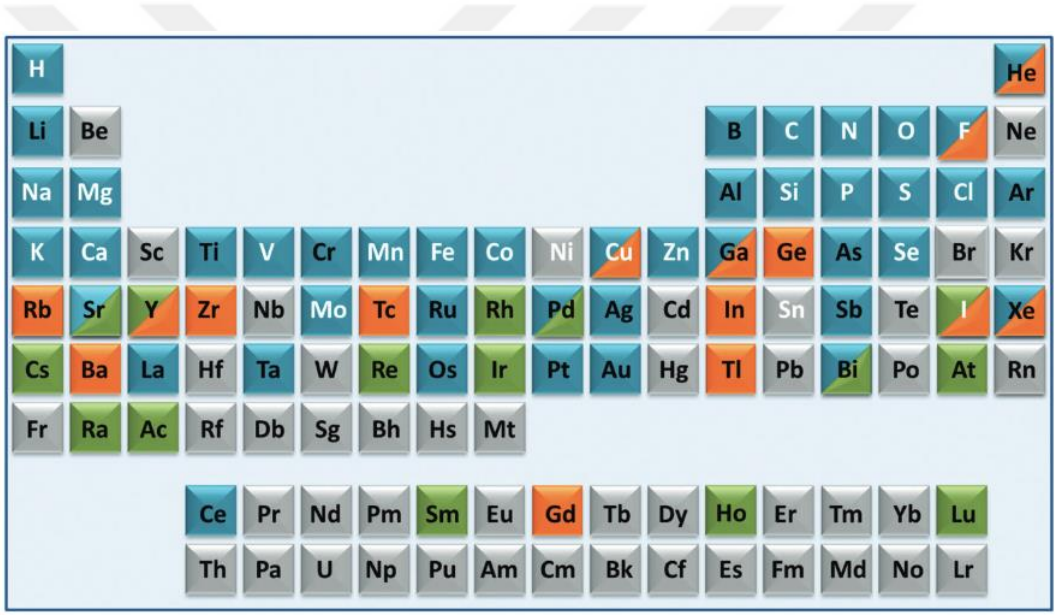


Figure 1.1 Periodic Table (Barry & Sadler, 2013).

The nucleus is generally in a state of stability, however, in the atoms with high atomic numbers, the nucleus stability is compromised due to an imbalance in the number of nucleons. To reach a stable state, the nucleus emits particles to balance the number of nucleons or emits energy packages, called photons, to release excessive energy caused by an imbalanced number of nucleons. These emitted particles or photons are called radiation (*Radiation Basics | NRC.Gov*, 2020).

1.1.1 Types of Radiation

In nature, radiation can be classified based on several properties. The classification can be either based on energy level, ionising radiation, or non-ionising radiation, or based on the physical form, electromagnetic radiation, or particulate radiation.

Electromagnetic radiation is the radiation that is in the form of waves without mass property. Electromagnetic radiations can be classified internally based on the wavelength of the propagating wave beginning from radio waves to X-rays and gamma-rays. The wavelength decreases, and as a result of the decrease in wavelength the frequency increases, from radio waves to gamma rays in the electromagnetic spectrum, as illustrated in Figure 1.2. As the frequency (ν) increases, the energy (E) level of the wave increases proportional to the increase in frequency based on Eq. 1.1 (h represents the Plank constant $h = 6.626 \times 10^{-34}$ J. s) (L'Annunziata, 2012).

$$E = h.\nu \qquad (1.1)$$

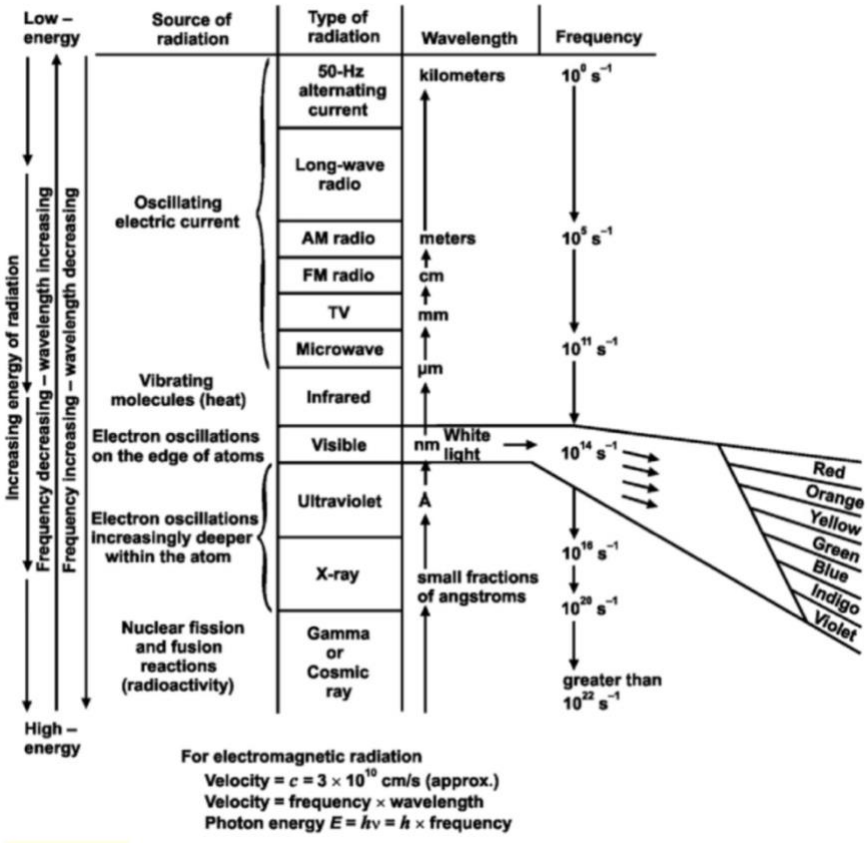


Figure 1.2 Electromagnetic Spectrum as Per Energy Levels (L'Annunziata, 2012).

The electromagnetic radiation from radio waves to ultraviolet waves does not have enough energy to interact with surrounding atoms to remove an electron from any of their external orbits. Yet, they can affect them by physical means like vibrating the atoms. However, due to the low wavelength and high frequency, the energy of X-rays and gamma rays is enough to remove electrons from their shells (Zamanian & Hardiman, 2005). The radiation types that are able to remove electrons from shells of surrounding atoms are known as ionising radiation and the other types, that are not able to remove electrons from their orbits, are known as non-ionising radiation.

The ionising and non-ionising waveforms and their exemplary effects are presented in Figure 1.3.

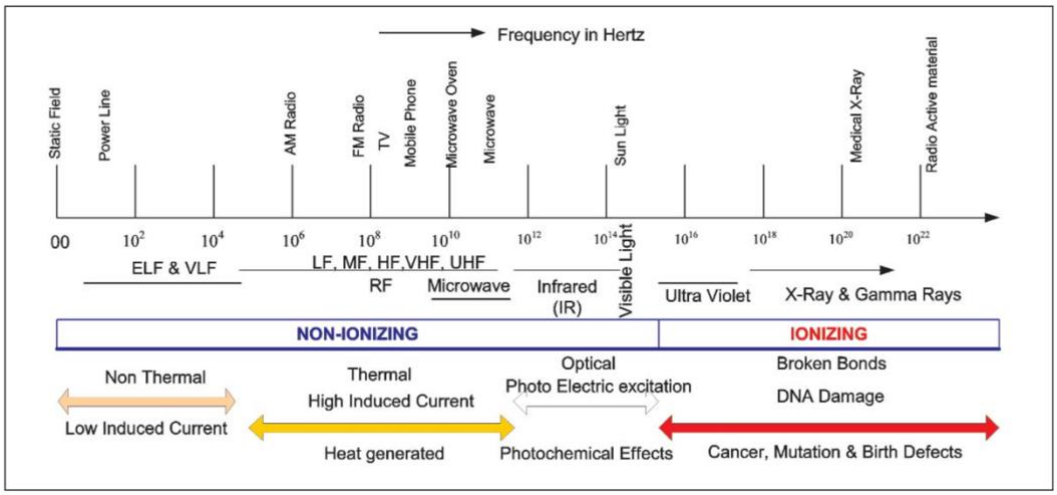


Figure 1.3 Non-Ionising and Ionising Radiation, and Their Exemplary Effects (Zamanian & Hardiman, 2005).

Apart from non-ionising radiation and electromagnetic ionising radiation, the radiation types that propagate as particles with a certain mass by the disintegration of radioactive nuclei are known as particulate radiation. The energy levels of these types of radiation are higher than X-rays and gamma rays. The properties of particulate radiation and gamma rays are explained in detail in the following section. Figure 1.4 is presented below to make a summary of radiation types.

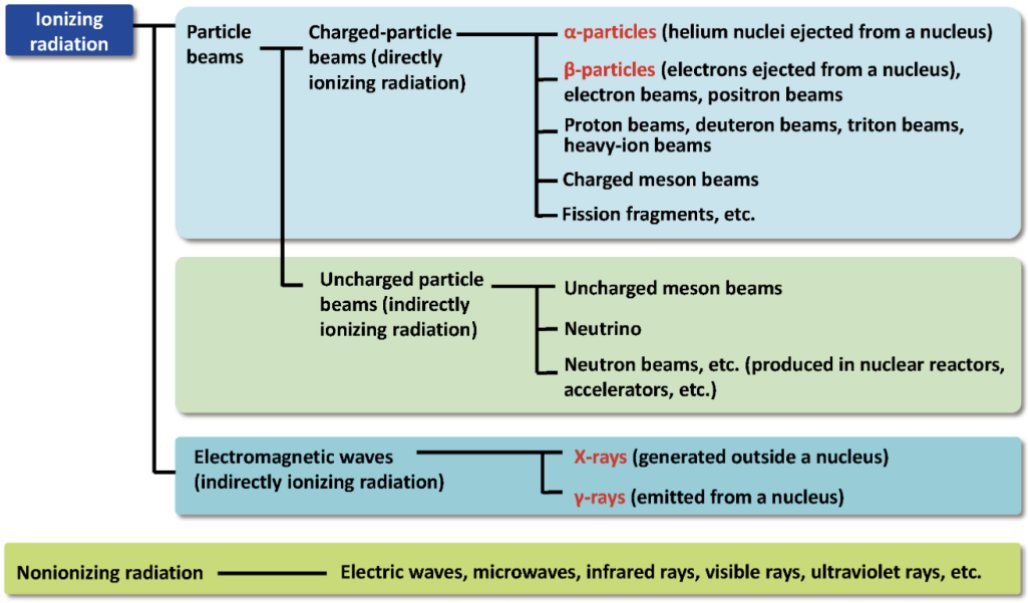


Figure 1.4 Summary of Radiation Types (*Types of Radiation [MOE]*, n.d.).

1.1.2 Radioactive Isotopes and Radioactive Decay

In some combinations of neutron and proton numbers, neutron numbers can be randomly equal while proton numbers are different, these pairs are called isotones and otherwise pairs are called isotopes.

Apart from stable nuclei placed in the periodic table, until today lots of isotopes were discovered and their radioactive properties and decay characteristics were analysed. The discovered and analysed isotopes are recorded in the Karlsruhe Nuclide Chart (KNC) based on their neutron and proton numbers. The latest version of KNC (10th version, 2018), presented in Figure 1.5, includes 4040 isotopes in total with the latest update in 2018 since it was first issued in 1958. In the chart, the horizontal axis represents the neutron number, and the vertical axis represents the proton number (or atomic number). The isotopes are represented as coloured boxes according to their radioactive emission characteristics, as represented right corner of KNC (Sóti et al., 2019).

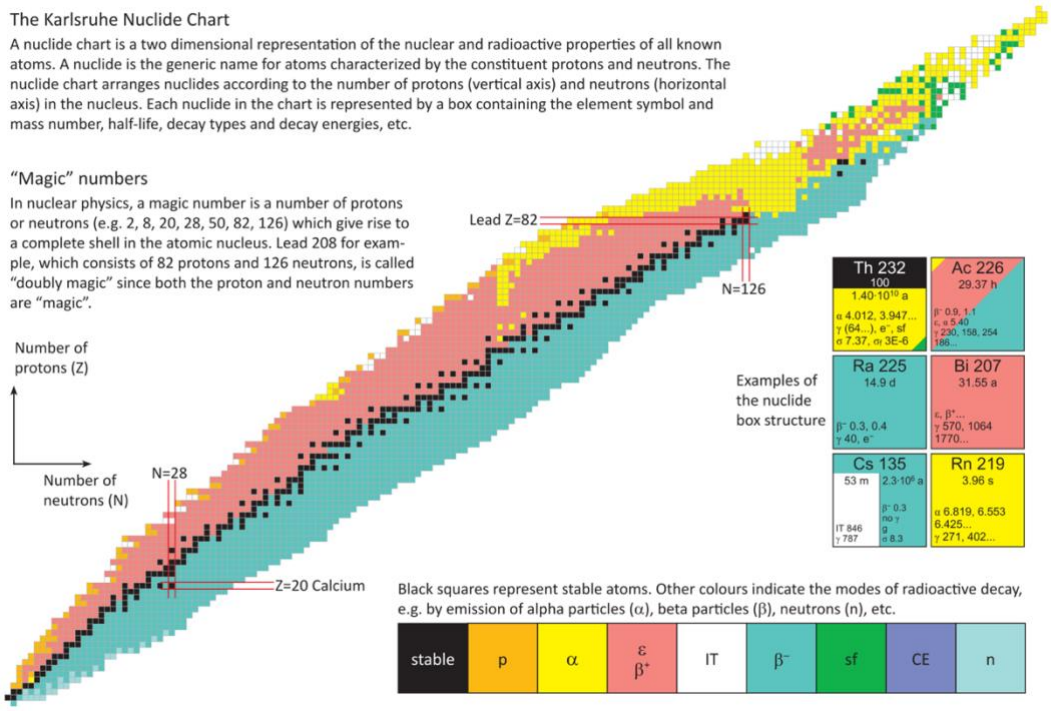


Figure 1.5 Karlsruhe Nuclide Chart 10th Edition, 2018 (Sóti et al., 2019).

Each unstable isotope in KNC emits electromagnetic or particulate radiation behaviour to become a stable nucleus is called radioactive decay, measured by the term half-life, and the tendency to undergo radioactive decay is called radioactivity (Kocher, 1981). The term radioactivity was identified by Antoine Henry Becquerel in 1896 using an experimental setup with uranium salts (Becquerel, 1896, 1903). The radioactive decay occurs randomly to reach a stable state of the nucleus by emitting alpha particles (α), beta particles (β^-or β^+), neutrons (n), protons (+) gamma rays (γ) or any combination of these radiations, as decay chains (L'Annunziata, 2012), as illustrated in Figure 1.6.

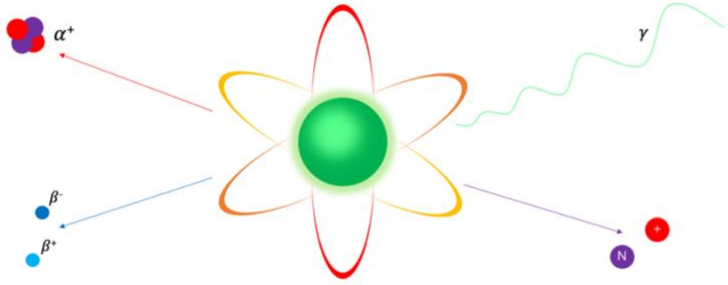


Figure 1.6 Illustration of Possible Decay Modes (Gibbons, 2019).

1.1.2.1 Radioactive Decay Notations

As mentioned before, each radioactive nucleus intends to become a stable nucleus by emitting excessive energy or unbalanced particles within, by radioactive decay. This radioactive decay of a radioactive nucleus is represented using the below decay notations. Each decay mode has its characteristic representation depending on the changing effect on energy level or atomic number or energy level. As illustrated in Figure 1.7, the decrease and increase in atomic number are represented as leftward and rightward arrows respectively, and the decrease in the energy is represented as a downward arrow.

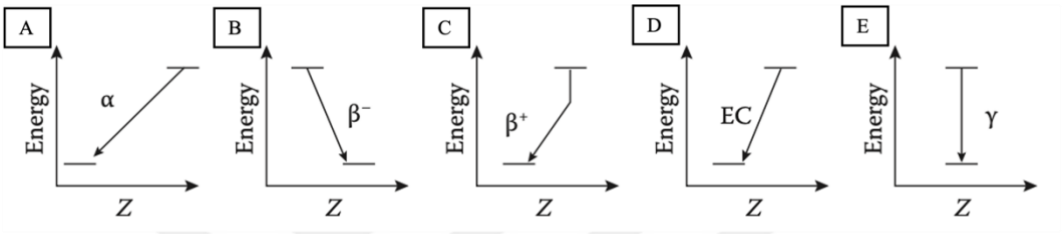


Figure 1.7 Decay Notations of Alpha (A), Beta Minus (B), Beta Plus (C), Electron Capture (D) And Gamma (E) Decays (Bryan, 2023).

As mentioned before, the radioactive decay process occurs randomly as a single emission or as a decay chain (Powsner & Powsner, 2006). In the case of decay chains, emissions of alpha, beta, and gamma radiations can occur and be schematised as the combination of decay notations of related decays presented in Figure 1.7.

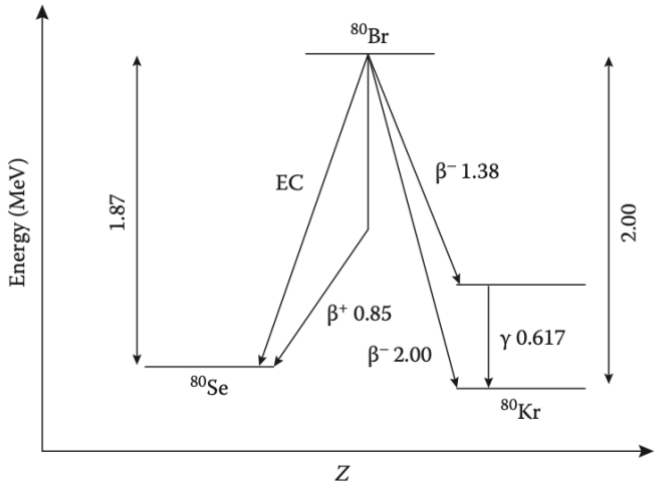


Figure 1.8 Radioactive Decay Routes of Br-80 Isotope (Bryan, 2023).

As an example, the possible radioactive decay routes of the Br-80 isotope are attached to Figure 1.8. According to the figure, Br-80 can follow either one of the following routes to become a stable given nucleus.

1- It can perform one beta minus decay along with one gamma decay to lose a total of 2 MeV energy to become a stable Kr-80 isotope.
2- It can perform one beta minus decay directly to lose 2 MeV energy to become a stable Kr-80 isotope.
3- It can perform one electron capture to lose 1.87 MeV energy to become a stable Se-80 isotope.
4- It can perform one gamma decay along with one beta plus decay to lose a total of 1.87 MeV energy to become a stable Se-80 isotope.

As radioactive decay is a random event, it is not possible to estimate when a certain atom decays, however, it is possible to estimate some portion of a group of atoms, like half of billions of radioactive atoms. The time span necessary to become half of a group of atoms stable is called half-life or $T_{1/2}$. The remaining half of the group decays after the same amount of time passes and this process continues until the number of unstable atoms in a group converges to zero. The activity characteristics can be schematised by a graph of an exponential curve, as in Figure 1.9.

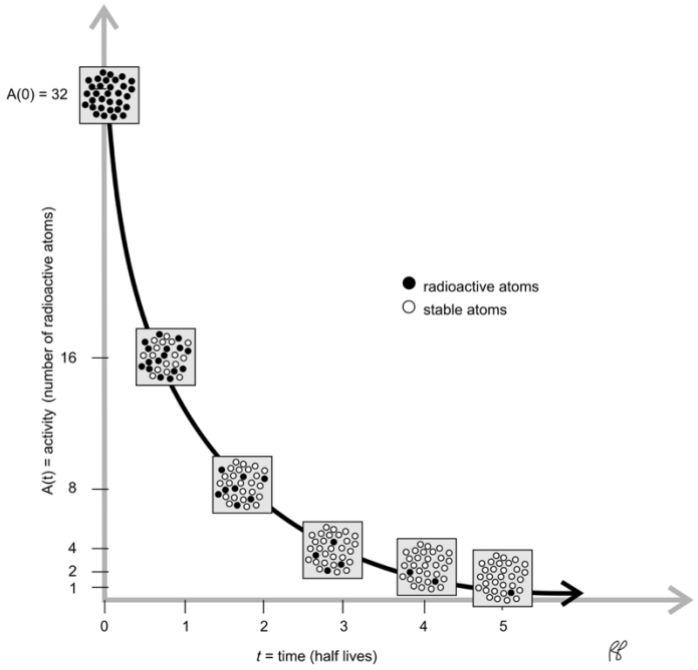


Figure 1.9 Decay Curve of Radioactive Atom A-32. Each Box Illustrates the Different Decay Steps, After One Half-Life (Powsner & Powsner, 2006).

The number of remaining unstable atoms can be found by equation (1.2), which is derived from the decay curves. In equation (1.2), A(t) represents the amount of remaining unstable atoms, A(0) represents the initial number of radioactive atoms and λ represents the decay constant, which is approximately calculated by division of 0.693 to half-life ($0.693/T_{1/2}$). By applying λ to equation (1.2), the equation is rewritten as given in equation (1.3).

$$A(t) = A(0)e^{-\lambda t} \tag{1.2}$$

$$A(t) = A(0)e^{-(0.693/T_{1/2})t} \tag{1.3}$$

The common and traditional unit of radioactivity is the curie (Ci), and the newer and SI-unit system-based unit is the becquerel (Bq). One becquerel represents one radioactive decay in a second. As the amount of radioactivity utilized in nuclear medicine is a million times one becquerel, the unit of MBq is generally used. The relationship between these units is summarized in Figure 10 (Powsner & Powsner, 2006).

One curie (Ci)	One millicurie (mCi)	One microcurie (μCi)	One bequerel (Bq)[a]	One megabecquerel (MBq)
	10^{-3} Ci	10^{-6} Ci	27×10^{-12} Ci	27×10^{-6} Ci
1×10^{3} mCi		10^{-3} mCi	27×10^{-9} mCi	27×10^{-3} mCi
1×10^{6} μCi	1×10^{3} μCi		27×10^{-6} μCi	27 μCi
37×10^{9} Bq	37×10^{6} Bq	37×10^{3} Bq		1×10^{6} Bq
37×10^{3} MBq	37 MBq	37×10^{-3} MBq	1×10^{-6} MBq	

[a] One becquerel equals one decay per second.

Figure 1.10 Conversion of Ci to Bq and MBq (Powsner & Powsner, 2006).

The radioactive decay is performed by emitting the following particulate or electromagnetic radiations.

1.1.2.2 Alpha Decay (α-decay)

By alpha decay, the parent atom, which can be classified as a heavy or superheavy radioactive isotope whose atomic number is over 82 in KNC, emits charged helium nuclei from its nuclei (Murshed, 2019) and was discovered by Rutherford in 1899 (Rutherford & Royds, 1899). Emitting helium means two protons and two neutrons

are ejaculated from the nucleus to become a stable nucleus, the ejaculation is performed as demonstrated in Figure 1.11.

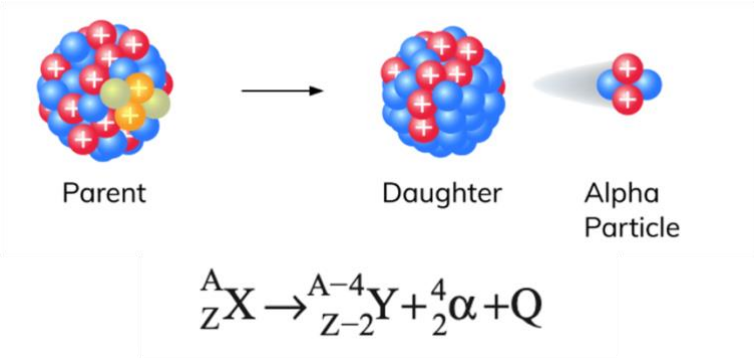


Figure 1.11 General Representation of a Parent Atom Facing Alpha Decay (Washington & Leaver, 2015).

In the above figure, ${}^{A}_{Z}X$ represents the parent atom, ${}^{A-4}_{Z-2}Y$ represents the daughter atom, ${}^{4}_{2}\alpha$ represents the emitted alpha particle (identical to helium nuclei) and Q represents the excessive energy emitted during the alpha particle which commonly appears as consecutive gamma-decay (Washington & Leaver, 2015).

As a result of being a heavy particle, which is composed of two protons and two neutrons, the alpha particles can propagate within short distances (41 mm in the air for 5.5 MeV), however, they can form ion pairs in gasses that they pass through by exciting the electrons from most outer orbits of gas atoms. This ion pair consists of a positively charged atom, an electron-losing atom, and removed electrons (Greene et al., 1972).

Since alpha particles have high-energy and low-penetration characteristics, they are preferred in treatment procedures like bone metastases (Cheetham & Petrylak, 2012), prostate cancer (De Vincentis et al., 2019; Morgenstern et al., 2020; Parker, Heidenreich, et al., 2018), targeted cancer treatment (Parker, Lewington, et al., 2018), and squamous cell carcinoma (Popovtzer et al., 2018).

1.1.2.3 Beta Decay (β-decay)

Beta decay occurs as a result of the ejaculation of negatively (conventional electrons) or positively (positrons) charged electrons from parent radioactive atoms. In the case of electron ejaculation, decay is called beta-minus (β^-) otherwise it is called beta-plus (β^+, positron). Beta decay occurs in proton-neutron-wise

imbalanced radioactive atoms. If the nucleus is proton-rich, it attempts to emit a positive charge by beta-plus (positron) emission along with a neutrino, as illustrated in Figure 1.12-A or captures an orbital electron to combine with a proton and turn it into a neutron. On the other hand, if the nucleus is proton-deficient, it attempts to emit a negative charge by beta-minus emission along with an antineutrino, as illustrated in Figure 1.12-B and converts a neutron into a proton (Welsh, 2006). In Figure 1.12, white circles represent the neutrons, red circles represent the protons, $\bar{\nu}$ represents antineutrino and ν represents neutrino.

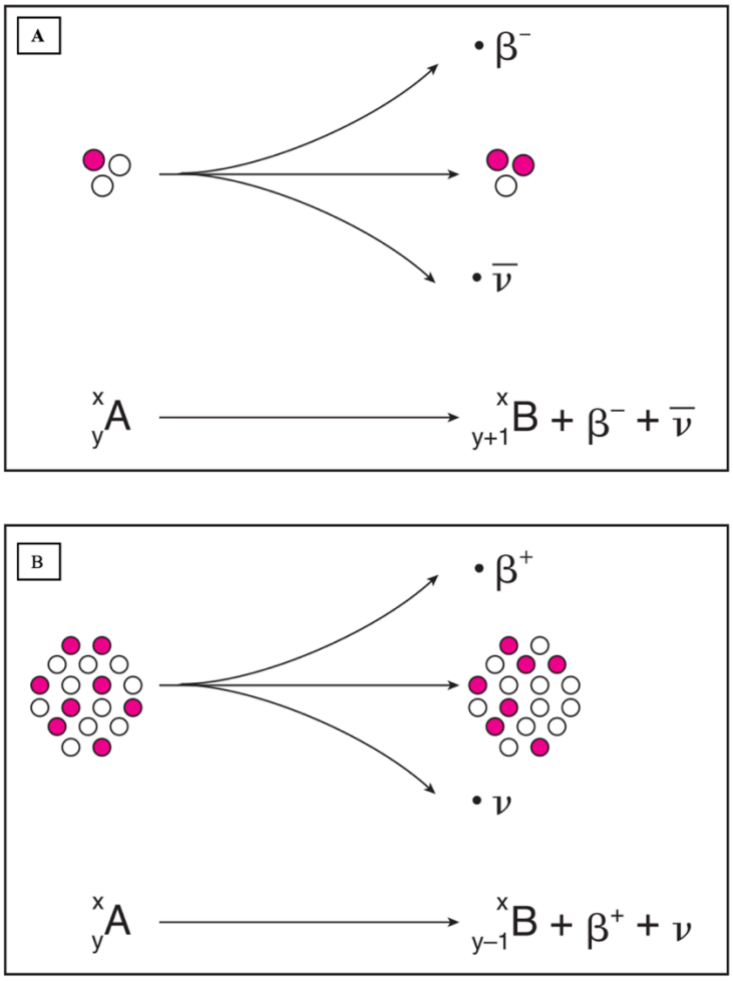


Figure 1.12 Illustration of Beta Decay. (A) Beta-Minus Decay. (B) Beta-Plus Decay (Welsh, 2006).

As beta radiation is rapidly diminished in biological tissue, it is used for decades in several clinical applications and procedures such as glaucoma surgery (Kirwan et al., 2009), radioimmunotherapy, thyroid ablation for benign and malignant disease, microsphere brachytherapy for malignant liver diseases, bone metastases (Welsh,

2006), treatment of primary and recurrent pterygia (Pajic & Greiner, 2005), prevention of restenosis after balloon angioplasty (Itali et al., 2001; King III et al., 1998; Serruys et al., 2002) and prevention of hyperplasia (Levitt et al., 2004). In addition to treatment options, beta-plus radiation is utilized in medical imaging applications for diagnostic and monitoring purposes in positron emission tomography (PET) (Shukla & Kumar, 2006; Welsh, 2006).

1.1.2.4 Electron Capture Decay (EC–decay)

Electron capture decay occurs if an electron is placed close enough to the nucleus to be captured, combined with a proton, and converted into a neutron along with the emission of a neutrino, so that in a nucleus with a higher number of protons than neutrons, as illustrated in Figure 1.13. As an orbital electron is ripped from its location, an electron from the higher-level shells will fill this gap in the lower-level shells. It results in the emission of characteristic X-rays and Auger electrons (Murshed, 2019). As a result of electron capture decay, the same result is obtained with positron decay (Washington & Leaver, 2015).

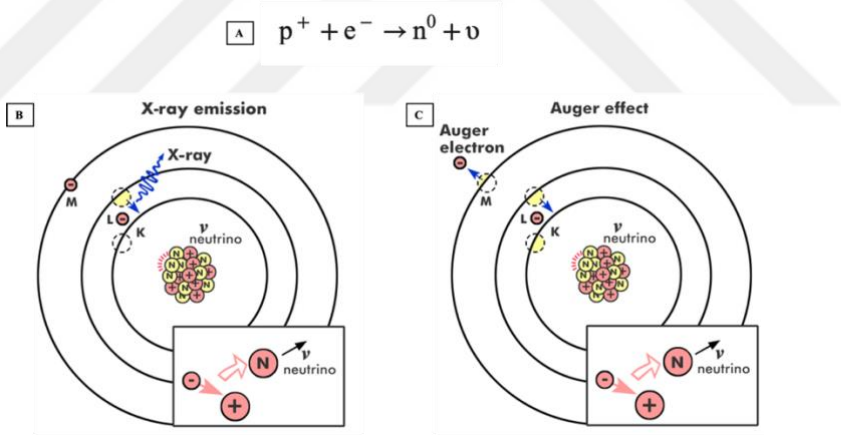


Figure 1.13 Illustration of Electron Capture. (A) Conversion Equation of Captured Electron to Neutron, (B) Illustration of Characteristic X-Ray Emission, (C) Illustration of Auger Effect (Martin & Godes, 2018).

1.1.2.5 Gamma Decay (γ-decay)

When the parent radioactive nucleus performs particulate radioactive decay, it may not directly become a stable atom and its daughter atom is realised as an excited atom. This excited realised daughter atom needs to emit excessive energy by gamma-decay, as illustrated in Figure 1.14 (Das & Ferbel, 2003).

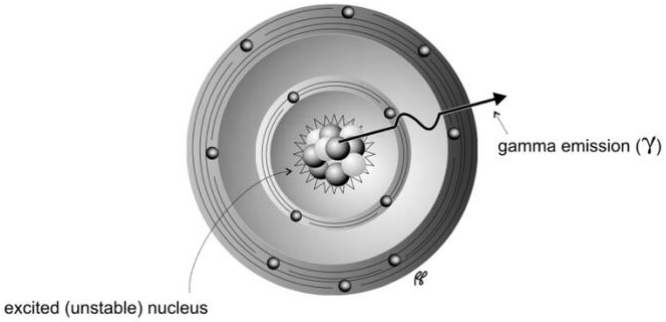


Figure 1.14 Illustration of Gamma Decay of an Excited Daughter Nucleus (Powsner & Powsner, 2006).

When an excited daughter atom is realised upon a particulate radioactive decay, its excited state is represented with the letter "m" next to the atomic number of the realised daughter atom, as illustrated in Figure 1.15.

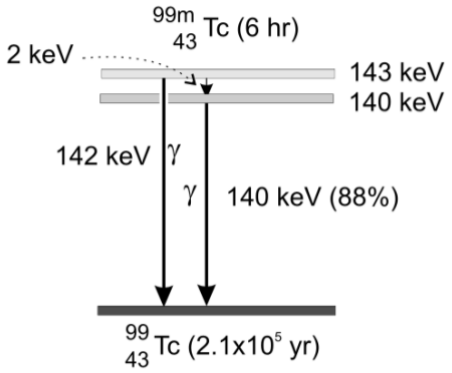


Figure 1.15 The Two Possible Gamma Decay Processes of Excited Tc-99m Atom to Become Stable Tc-99 Atom (Powsner & Powsner, 2006).

As a result of gamma decay, the excited daughter atom does not lose atomic weight, it only releases its excessive energy, therefore decay notation of gamma decay is only a downward arrow as shown in Figure 1.7-E (Das & Ferbel, 2003).

1.2 Nuclear Medicine

Nuclear medicine is a medical speciality that utilises radiation and focuses on the treatment of several pathologies, and functional or molecular imaging of biological structures. The radiation sources utilised in nuclear medicine are called radiopharmaceuticals. These radiopharmaceuticals are designed specifically for related purposes, related targeted tissue, and characteristics of emitted radiation. Once they are administrated to the patient, due to being designed specifically for

targeted tissue, they accumulate within the tissue and achieve their intended purpose, which is treatment or imaging as will be explained in the following sections.

1.2.1 Interactions of Radiation with Surrounding Matters

When electromagnetic radiation, travels through any matter in the form of energy packages which are called photons, it interacts with its surrounding atoms. The interaction with the surrounding atoms depends on the total energy of the incident photon. Within the energy range of 10 keV to 10 MeV, the photoelectric effect, Compton scattering, and pair production interactions are observed mostly. Due to the strength of the incident photon, the observed physical phenomenon differs as will be explained in the following sections.

Besides electromagnetic radiation types like gamma rays, particulate radiations interact with matter as well. They interact more easily than electromagnetic radiations due to being charged and relatively heavier particles. Due to their charges, they interact with surrounding atoms, and they eject electrons from their orbits and cause ionising effects due to electrostatic repulsive or attractive forces caused by being charged particles (Powsner & Powsner, 2006).

In comparison between the ionising effects of particulate and electromagnetic radiation, particulate radiation has a higher capacity to ionise the surroundings than electromagnetic radiation in short distances. Because of having higher masses and being charged particles, they are not able to propagate in longer distances within surrounding matters, therefore they are known as non-penetrating radiation when they are compared with electromagnetic radiation (Powsner & Powsner, 2006).

1.2.1.1 Photo Electric Effect

In the photoelectric effect, an incident photon whose energy is higher than the binding energy of the target electron collides with the electron and transfers all its energy to that electron to remove it from its shell. As a result of the photoelectric effect, a scattered electron with an energy level of E_e is released from its orbit as illustrated in Figure 1.16. The kinetic energy equation of the photoelectric effect is as in the following equation (Ahmed, 2007).

$$E_\gamma = E_B + E_e \tag{1.4}$$

In equation (1.4), E_γ represents the energy of the incident photon, E_B represents the binding energy of the target electron and E_e represents the kinetic energy of resulting travelling electron.

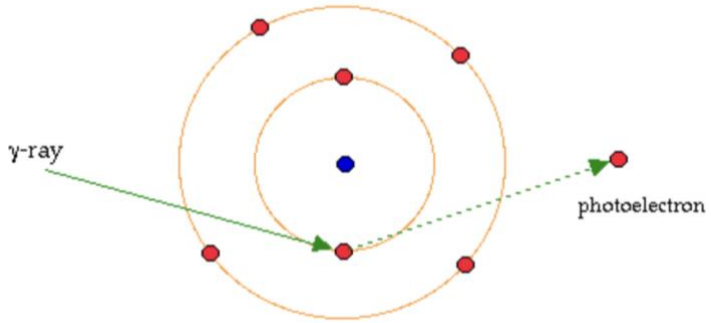


Figure 1.16 Illustration of The Photoelectric Effect (*Basic Physics of Nuclear Medicine/Interaction of Radiation with Matter - Wikibooks, Open Books for an Open World*, n.d.).

As the target electron is removed from its original location, an electron from one of the outer shells fills the generated vacancy. As a result of this vacancy filling, a characteristic X-ray is emitted with a certain energy level depending on the shell of the filling electron, or an auger electron is released from one of the outer shells of the atom, as illustrated in the following figure.

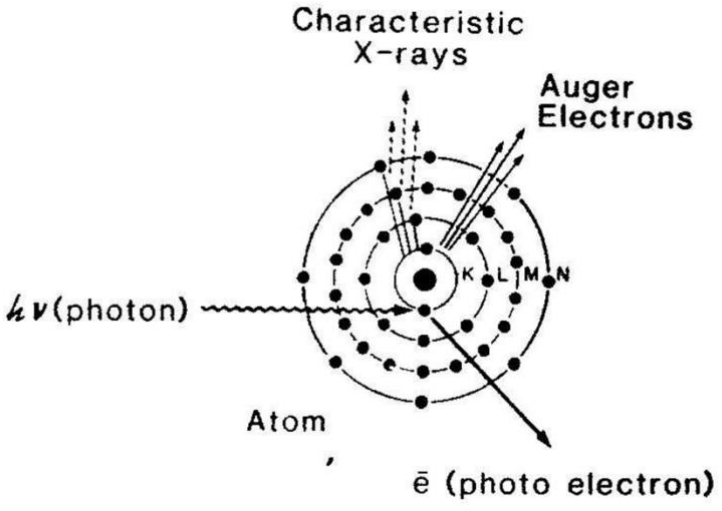


Figure 1.17 Illustration of The Photoelectric Effect and Consecutive Events, Characteristic X-Ray and Auger Electron Emission (Rahman, 2017).

1.2.1.2 Compton Scattering

Compton scattering occurs when the incident photon has more energy than the binding energy of the target electron and does not transfer its all energy to the electron and scattered along with it with some part of its initial energy, as summarized in Figure 1.18. In Compton scattering the level of transferred energy to electron from photon is directly proportional to the scattering angle, so it means that the larger scattering angles result in larger energy transfer to electron, therefore, the maximum energy transfer occurs at 180 ° scattering angle, which is called back-scattering (Qiao et al., 2021; Shaffer et al., 2016).

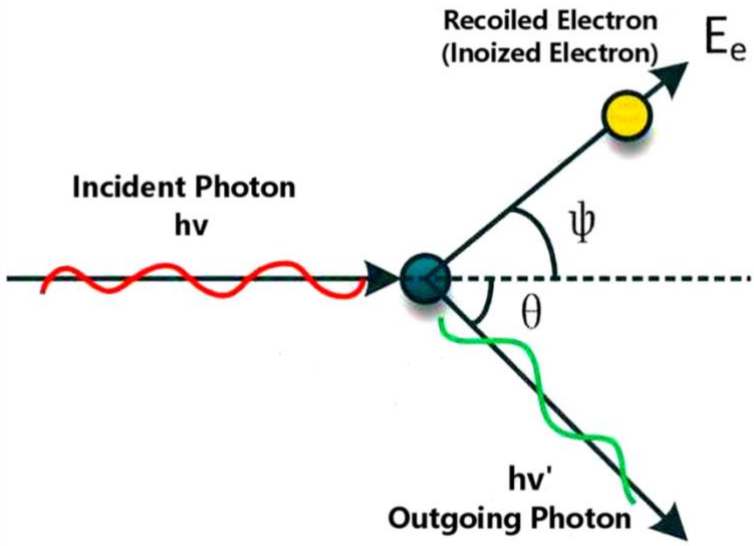


Figure 1.18 Illustration of The Compton scattering (Qiao et al., 2021).

The energy equation of the Compton scattering phenomenon is presented in equation (1.5).

$$E_\gamma = E_B + E_e + E'_\gamma \qquad (1.5)$$

In the above equation, E_γ represents the energy of the incident photon, E_B represents the binding energy of the target electron, E_e represents the kinetic energy of the resulting travelling electron and E'_γ represents the scattered photon upon collision.

As in the photoelectric effect, the vacancy caused by the collusion is filled by another electron from outer shells and again the emission of characteristic radiation or release of an auger electron is realised.

1.2.1.3 Pair Production

In pair production cases, the incident photon must have at least 1.02 MeV energy, which is equal to two-fold of the energy of the electron's rest mass ($2mc^2 \cong 1.02\ MeV$), and photon should pass near to charged mass, like the nucleus, to generate the anti-particle of the target electron. When the photon propagates within the electrical field of the nucleus, the energy of the photon transforms into mass and generates one electron (e) and one positron (e^+) (Chandra & Rahmin, 2018; Leroy & Rancoita, 2009), as in Figure 1.19. The energy of the incoming photon is divided between the generated electron and positron, so the energy equation in pair production is as in equation (1.6).

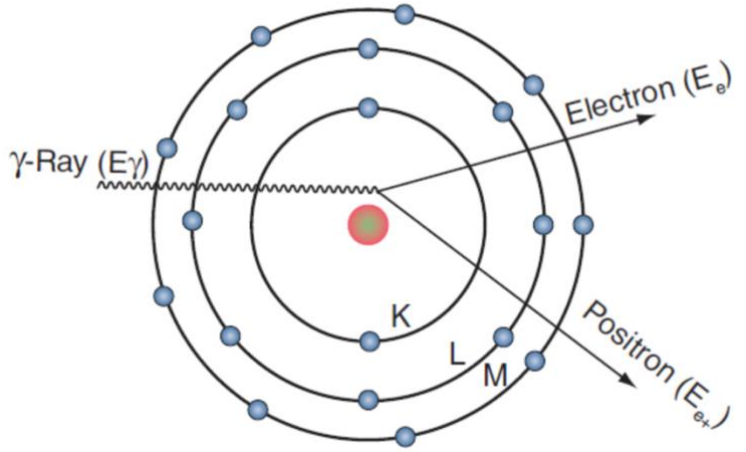


Figure 1.19 Illustration of Pair Production (Chandra & Rahmin, 2018; Shaffer et al., 2016).

$$E_\gamma = E_e + E_{e^+} \qquad (1.6)$$

1.2.1.4 Annihilation

In addition to photons, particles, like electrons and positrons, can cause events if they encounter their anti-matters and transfer all of their kinetic energy. Although anti-matter-encountering characteristics are the same in electrons and positrons, positrons cause an annihilation event which occurs when a positron encounters with an electron, which is its anti-matter. This encountering event creates instability and leads to the creation of two gamma rays propagating in opposite directions with 511 keV energy, as illustrated in Figure 20. The gamma rays may be emitted in several

different directions, but they are always opposed to each other, in all those possible directions (Chandra & Rahmin, 2018; Leroy & Rancoita, 2009; Milano et al., 2013).

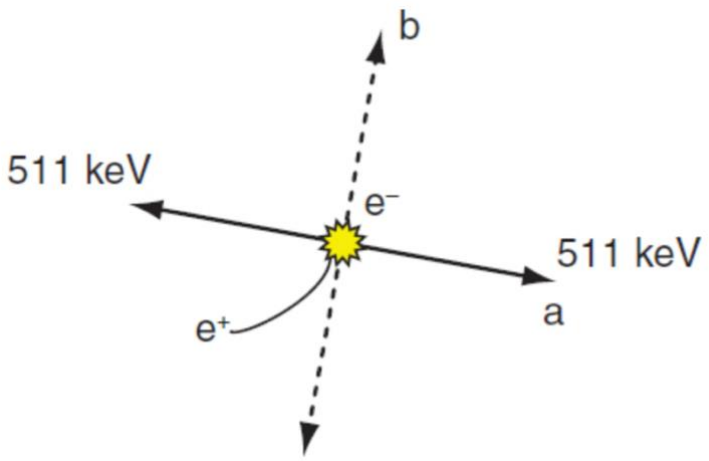


Figure 1.20 Illustration of Annihilation of The Positron (Chandra & Rahmin, 2018).

In the above figure, a and b represent the examples of possible two directions for the gamma-ray emission.

This phenomenon is utilised in positron emission tomography (PET) devices to capture molecular images of biological structures.

1.2.2 Radiopharmaceuticals in Nuclear Medicine

The mechanism of action of nuclear medicine includes administrating radioactive materials, in other words, radionuclides or radioactive isotopes, to patients to treat specific diseases or monitor the functions of biological structures. Upon the administration of radionuclide, it travels through the body until it reaches the desired biological structure and starts accumulation. Due to the characteristic of the biological substrate, or carrier molecule, which is specific for each targeted biological structure, the accumulation takes place. To perform the specific purpose of nuclear medicine, monitoring, or treatment, the carrier molecule is combined with radionuclide. As in carrier molecules, the radionuclide is also selected specifically for the purpose based on its chemical properties, half-life, and energy level (Zimmermann & Pouchot, 2019).

The radiolabelled molecule, which is intended to be used in several vivo applications, is known as radiopharmaceutical. For each in vivo application, mainly radiopharmaceuticals consist of two critical parts which both can be application

specific. The first part known as molecular structure is selected based on suitability for targeted biological structure and according to its pharmacokinetic and pharmacodynamic characteristics, accumulation within tissue is obtained. The other part known as radioactive nuclide is selected according to intended to be emitted radiation characteristics and responsible for emitting radiation for diagnostic or therapeutic purposes. The molecular structure, the part that is not radiolabelled, allows pharmaceuticals to be recognized and accumulated based on several factors like antigens, enzymes, or receptors by targeted biological, in vivo, structure (Wadsak & Mitterhauser, 2010).

The therapeutical application fundamentally depends on admitting radionuclides to the desired biological structure to be treated like cancerous tissues. The admission of radiation might be intravenously, systematically, locoregionally, or from an external source depending on the application. In therapeutic applications generally, radiopharmaceuticals with gamma-ray or alpha-ray emission characteristics are utilized. The yttrium-90, iodine-131, samarium-153, astatine-211, radium-223 thorium-227 are the main radiation sources used in radiopharmaceuticals for therapeutic applications of nuclear medicine (Sgouros et al., 2020).

Furthermore, as used in therapeutic applications, several different radiopharmaceuticals are utilized within diagnostic applications. The diagnostic application of nuclear medicine basically depends on the idea of monitoring emitted radiation from radionuclides of radiopharmaceuticals in the human body. Due to molecular structure, pharmaceuticals reach the targeted area and due to the radiation emission characteristics of radionuclides allow physicians to monitor the desired biological structure via positron emission tomography (PET), single photon emission computed tomography (SPECT), or gamma camera devices. Radiopharmaceuticals are used in PET mainly in the form of molecular structures combined with positron-emitting radionuclides (Wadsak & Mitterhauser, 2010). Due to their positron-emitting characteristics, generally, fluorine-18 ([^{18}F]-FDG) is preferred for PET. In addition to fluorine-18, oxygen-15 and carbon-11-based compounds are used in PET applications to monitor blood flow measurement and neural disorders respectively. On the other hand, in SPECT radionuclides that have gamma-ray emitting properties, are preferred like iodine-123, technetium-99m,

xenon-133, thallium-201, and indium-111 to monitor seizures, bone deficiencies, and infection (Crișan et al., 2022).

1.3 Therapeutic Applications of Nuclear Medicine

Nuclear medicine is an emerging medical speciality of modern healthcare, it revolutionized diagnostic and therapeutic approaches to an uncountable medical condition. Utilizing the unique properties of radiopharmaceuticals, nuclear medicine offers a variety of applications. From non-invasive diagnosis of complex diseases to targeted treatment strategies, nuclear medicine has become indispensable in providing clinicians with invaluable insights into the functional and molecular aspects of the human body. Through techniques such as positron emission tomography (PET), single photon emission computed tomography (SPECT), and targeted radionuclide therapy, nuclear medicine has allowed the way for personalized medicine, enabling tailored interventions that enhance patient outcomes and quality of life.

The discovery of the therapeutic applications of radiation was made in the 1900s by Henri Becquerel. After he faced skin inflammation caused by a radium bar that he put in his pocket, radiation started to be used in therapeutic medicine. Upon its discovery of being used in therapeutic medicine, radiation played an important role in several clinical applications (Dash et al., 2014; FORRER et al., 2006; Hoefnagel, 1991; HOEFNAGEL, 1998; NAKABEPU & NAKAJO, 1994; Yeong et al., 2014).

In therapeutic nuclear medicine, the selection of the radiation source plays a crucial role, and the selection depends on the physical characteristics such as half-life, decay mode or energy level of radiation (HOEFNAGEL, 1998; Troutner, 1987), and biochemical characteristics like suitability for targeted tissue and toxicity, of radionuclides (Kassis & Adelstein, 2005). Table 1.1 presents some examples of commonly used radiation sources and their characteristics with their indications. After evaluation of those criteria, the source should be the one with an optimal half-life, radiation type and carrier molecule for the targeted pathology. In general, for the larger tumours, α- or β-ray-emitting particles are selected and for small tumours or small clusters of cancer, auger electron-emitting particles are selected due to their high ionising effect in short propagation distances (in millimetres) (Ersahin et al., 2011).

Table 1.1 Characteristics of Some Radionuclides Utilized in Therapeutic Nuclear Medicine (Yeong et al., 2014).

Radionuclide	Physical half-life	Mode of decay	Principal energy level (keV)	Daughter nuclide	Clinical Indications
^{32}P	14.26 d	β^-	1710	^{32}S	Polycythemia vera, cystic craniopharyngioma, PVNS
^{89}Sr	50.53 d	β^-	1496	^{89}Y	Painful bone metastasis
^{90}Y	64.10 h	β^-	2280.1	^{90}Zr	Hepatic metastasis, PVNS, RIT for NHL
^{117m}Sn	13.60 d	IT	130*	^{117}Sn	Bone tumour treatment
^{131}I	8.02 d	β^-	606	^{131}Xe	Hyperthyroidism, thyroid cancer, RIT for NHL and neuroblastoma
^{186}Re	3.72 d	EC, β^-	1069.5	^{186}W	Painful bone metastasis, painful arthritis
^{188}Re	17.00 h	β^-	2120.4	^{188}Os	Painful bone metastasis, rheumatoid arthritis, RIT for various cancer treatments
^{223}Ra	11.44 d	α	5979.2	$^{219}Rn^*$	Bone metastasis

In addition, the selection of biological carriers is as important as radiation emission characteristics. Because it affects the radionucleus intake rate and duration (Qaim, 2001). By selecting of optimal combination of biological carrier molecules and radionuclides, radiopharmaceuticals are prepared to be used to treat intended pathology. The commonly used radiopharmaceuticals for therapeutic purposes are presented in Table 1.2.

Table 1.2 Common Radiopharmaceuticals in Therapeutic Nuclear Medicine (Yeong et al., 2014).

Radiopharmaceutical	Targeting mechanism	Clinical indication
^{131}I-iodide	Thyroid hormone synthesis	Differentiated thyroid cancer, Graves' disease, hyperfunctioning nodules
^{90}Y-microspheres	Intravascular trapping	Liver metastasis, hepatocellular carcinoma
^{89}Sr-chloride	Calcium analogue	Bone pain palliation
^{153}Sm-EDTMP	Chemo-adsorption	Bone pain palliation
^{90}Y-octreotide	Somatostatin receptor binding	Neuroendocrine tumours
^{131}I-MIBG	Active transport into neuroendocrine cells and intracellular storage	Neuroblastoma, pheochromacytoma, carcinoid, paraganglioma, medullary thyroid carcinoma

1.4 Diagnostic Applications of Nuclear Medicine

In the field of modern medicine, diagnostic nuclear imaging stands at the forefront of precision healthcare, offering unparalleled insights into the inner workings of the human body. By monitoring the energy of radioactive tracers and advanced imaging technologies, diagnostic nuclear medicine has revolutionized the way clinicians detect, diagnose, and monitor a diverse range of medical conditions. From assessing organ function and blood flow to detecting cancerous lesions and neurological disorders, nuclear imaging modalities such as positron emission tomography (PET), single photon emission computed tomography (SPECT), and hybrid imaging techniques (like SPECT/CT, PET/CT, PET/MRI) have become indispensable tools in the diagnostic armamentarium. With their ability to provide functional and molecular information, these techniques offer clinicians a comprehensive understanding of disease pathology, enabling timely interventions and personalized treatment strategies.

1.4.1 Anger Camera (Gamma Camera) and Single Photon Emission Computed Tomography (SPECT)

Gamma cameras and SPECT focuses on monitoring gamma radiation emitted by the administrated radiotracers (i.e., ^{99m}Tc, ^{111}In and ^{123}I) by physicians to patients. To do so, a scintillation device is utilized. The first radiation-detection system, which is called the Anger Camera (in other words gamma camera) and schematized in Figure 1.21, was discovered by Harold Anger in the 1950s and its design was revolutionised over previous rectilinear scanners. This system basically includes a collimator for the restriction of gamma rays from the source; a crystal (usually made of NaI), for converting the gamma rays to light; a photomultiplier for increasing the number of photoelectrons received from the crystal and several electronic components for image acquisition, processing, etc. (Khalil, 2011; Powsner et al., 2013).

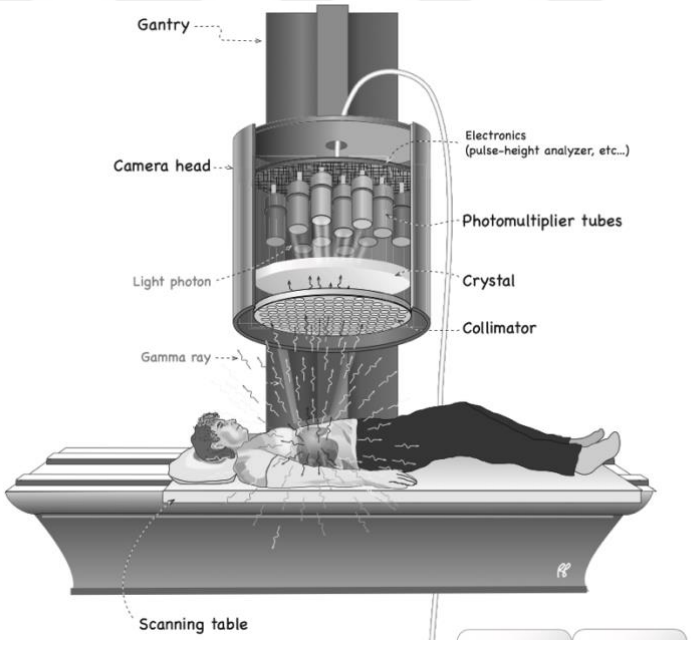


Figure 1.21 Illustration of Anger Camera (Powsner et al., 2013).

SPECT and gamma cameras work on the same principles. The only difference is in the dimensions of the acquired image. In gamma cameras, the image is two-dimensional while, in SPECT it is three-dimensional due to the rotational movement of the camera head (including collimator, crystal and photomultiplier and illustrated in Figure 1.22) (Khalil, 2011; Razibul Hasan et al., 2017). In SPECT

systems generally, more than one gamma camera, preferably pairs of cameras, are utilized and rotated around the patient. (Najam et al., 2023).

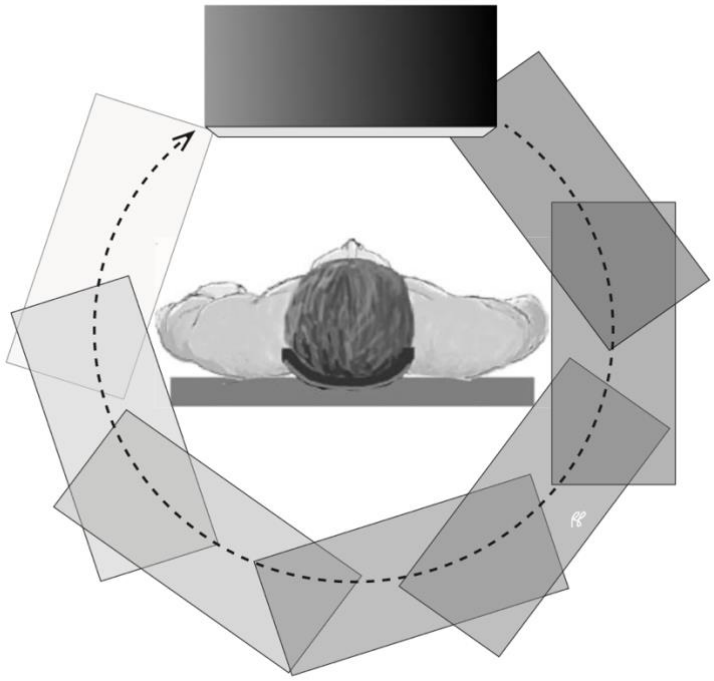


Figure 1.22 Illustration of Rotating SPECT Cameras Around Patient (Bushberg, 2012).

The major intended use of gamma cameras and SPECT systems is to obtain 2D or 3D (depending on the system) functional images of the brain, heart, respiratory system, liver and kidney (Razibul Hasan et al., 2017; Roth et al., 2022).

Even though SPECT's working principle depends on existing gamma cameras utilized with its design, its performance indicators slightly differ from gamma cameras. While the performance indicators of SPECT rely on spatial resolution, sensitivity, image uniformity and contrast, and attenuation, the performance indicators of gamma cameras depend on spatial resolution, energy resolution, detection efficacy, image uniformity and image contrast (Lancaster & Hasegawa, 2017).

1.4.2 Positron Emission Tomography (PET) – PET/CT – PET/MRI

PET is an emerging and popular molecular imaging technique in nuclear medicine as gamma cameras and SPECT systems. However, unlikely in those systems, the action mechanism of PET does not depend on single photon detection, it depends

on the detection of the produced pair of photons travelling in opposite directions. These pair of photons are produced after the annihilation process between a beta plus (positron) particle and its anti-matter (electron) in biological tissue. When a positron with an energy level higher than 1,02 MeV encounters an electron, it annihilates and creates two photons that are travelling in opposite directions with equal levels of energy, which are at least 511 keV. The ring-shaped PET detector placed around the patient detects this pair of photons and converts them into molecular images (Bailey & Townsend, 2005; Bushberg, 2012; Lancaster & Hasegawa, 2017). The PET imaging process illustrated in below Figure 1.23.

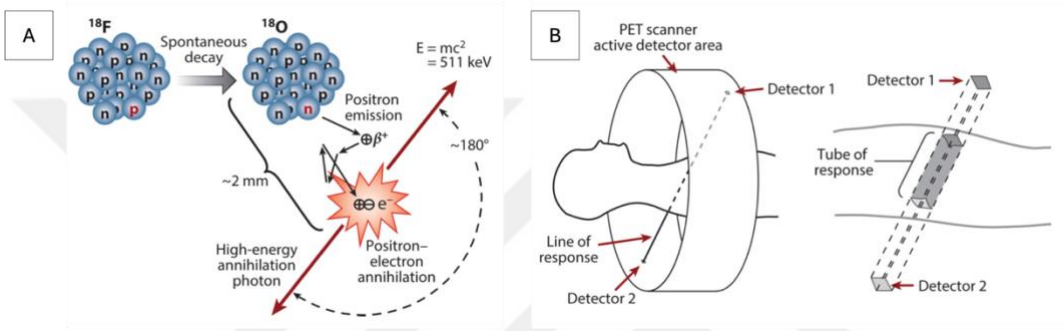


Figure 1.23 Illustration of Photon Detection in PET. (A) Illustration of Positron Annihilation, After Positron Decay of F-18 To O-18. (B) Photon Detection by The Corresponding Detector Pair in The Detector Ring of The PET Camera Including Representation of Line of Response and Tube of Response (Saturnino Guarino & Martelli, 2018).

In PET systems, radiopharmaceuticals like F-18 (FDG), C-11, O-15 and Ga-68 are preferred because of their positron emission characteristics during their radioactive decay process (Najam et al., 2023). Moreover, the camera systems of PET are uniquely designed, as shown in Figure 1.24 and separated with lead or tungsten septa to detect coincident pair photons simultaneously. The septa separators are utilized to prevent scattering in the transverse plane and avoid the use of electronic collimators (Townsend, 2008).

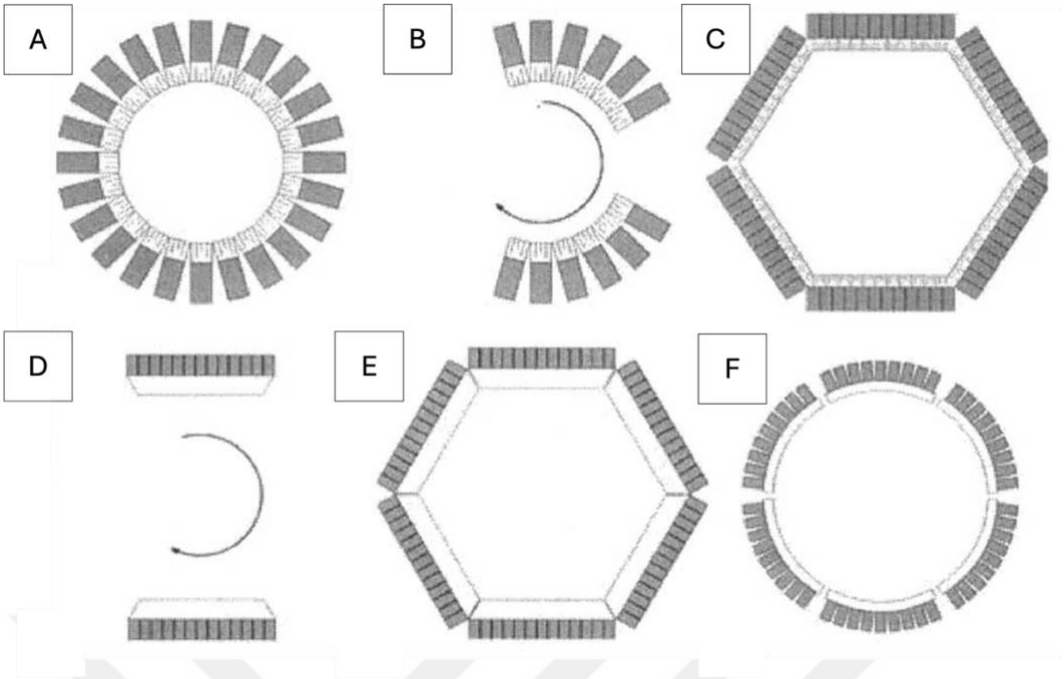


Figure 1.24 Configurations of Detectors in PET Systems. (A) Multiple Full Rings Configuration of Detector Blocks, Each Containing Discrete, Small-Area Detector Elements. (B) Multiple-Partial Ring Configuration of Detector Blocks, Each Composed of Small-Area Detector Elements. (C) Hexagonal Array Configuration of Detector Banks, With Each Bank Consisting of Small-Area Detector Elements. (D) Large-Area Detectors Configuration Which Placed as Opposed to Each Other, such as Anger Cameras. (E) Hexagonal Array Configuration of Detector Banks, with Each Bank Consisting of Large-Area Detector Elements. (F) Circular Configuration of Six Large-Area and Curved Detectors (Zanzonico, 2004).

The detectors in PET systems, which are placed between those rings in circular or hexagonal configurations, produce a response if and only if both coincidence pairs of detectors are actuated by annihilated photons (Zanzonico, 2004). In detectors, dense scintillation crystals like LSO, BGO and GSO are preferred to increase the acquisition performance (Melcher, 2000). In the history of scintillation detectors, in the first designs of PET detectors thallium-activated sodium iodide (NaI(Tl)) was used, after discovering the advantages of bismuth germanate (BGO) over NaI(Th) in the 1970s, BGO started to be used in PET systems. After the discovery of robust characteristics of gadolinium oxyorthosilicate (GSO) and lutetium oxyorthosilicate (LSO) in the 1990s, scintillators have started to be designed using these materials. Both these designs are enhanced with cerium to improve the image acquisition

performance of the PET system (Townsend, 2008). Furthermore, each photomultiplier in the PET system is coupled with detectors (Ariño et al., 2013).

Major performance-effecting criteria in PET systems are spatial resolution, sensitivity and attenuation correction (Najam et al., 2023; Powsner et al., 2013). Although PET imaging is one of the most promising methods among the functional imaging modalities, to provide superior diagnostic information to physicians, functional information obtained from PET and anatomical information obtained from computed tomography (CT) or magnetic resonance imaging (MRI) are combined in hybrid imaging modalities, PET/CT or PET/MRI and they become emerging topics in the medical imaging field (Sauter et al., 2010; Townsend & Cherry, 2001).

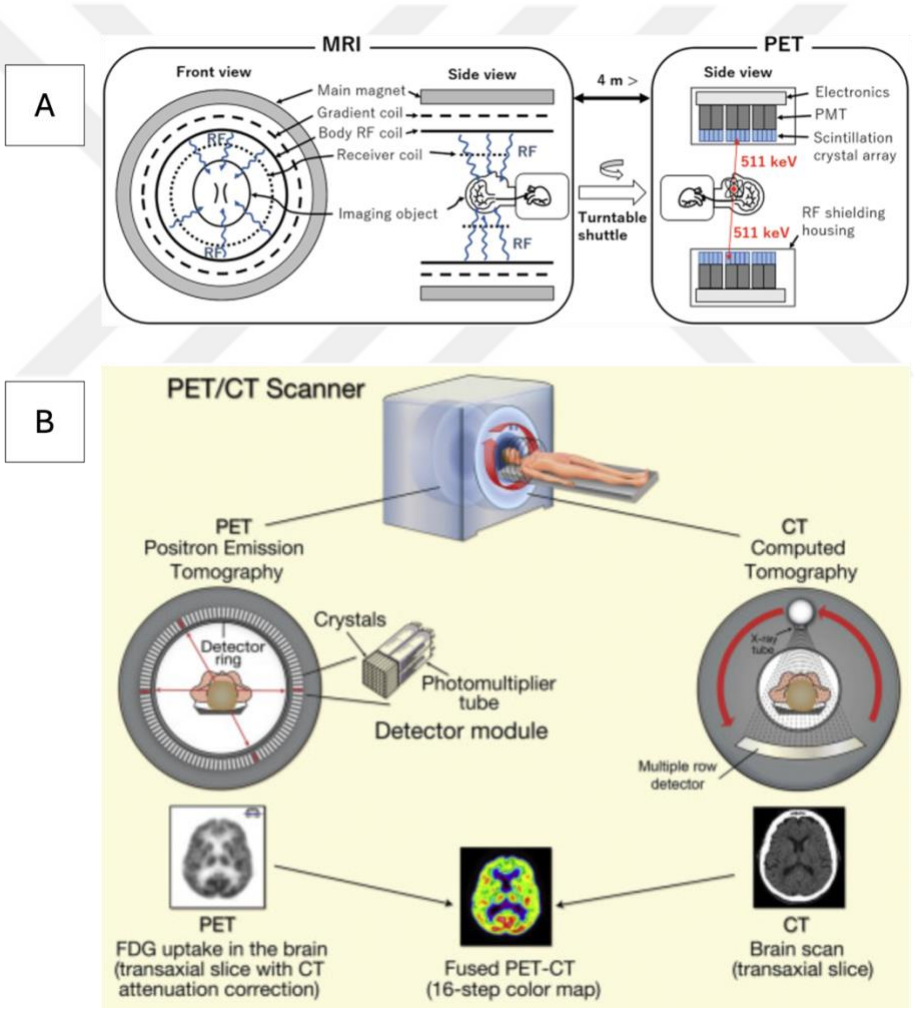


Figure 1.25 Illustrations of PET/MRI and PET/CT Hybrid Imaging Modalities. (A) PET/MRI modality (Kang & Yamaya, 2021). (B) PET/CT modality (Lameka et al., 2016).

The integration of anatomic information from MRI and functional information from PET allowed significantly improved image reconstruction algorithms and motion correction techniques for PET/MRI images (Ehman et al., 2017), whose working principle was illustrated in Figure 1.25-A. In addition to this, the integration of anatomical information from CT and functional information from PET provided improved localisation and better attenuation correction for PET/CT images (Tsai & Liu, 2021), whose working principle was illustrated in Figure 1.25-B.

Although integrated systems have advantages over lean imaging methods and each other, they also have individual limitations. The following tables, Table 1.3 and Table 1.4, summarize the individual advantages and limitations of PET/CT and PET/MRI respectively.

Table 1.3 Advantages and Limitations of PET/CT (Ehman et al., 2017).

Advantages	Limitations
Widely available	Limited soft tissue contrast
Established imaging protocols	Fast CT exam does not provide extra time for PET acquisition
Evidence proven indications	IV contrast not routinely used
Familiarity among ordering providers	If focused MRI needed, must be additional exam
Quantitative accuracy well established	Ionizing radiation from CT component
Imaging of small pulmonary nodules	-
Exams performed in as little as 30 minutes	-

Table 1.4 Advantages and Limitations of PET/MRI (Ehman et al., 2017).

Advantages	Limitations
Improved soft tissue contrast	Limited availability
Added value of diffusion weighted imaging	Protocols and indications still in development
Increased available time to collect PET data	Require technologist knowledgeable in both nuclear medicine and MRI
Better motion correction	Quantitative accuracy still being determined
Convenience and time savings with combined exams	Exams may take 1 hour or longer
Use of MRI specific contrast agents	Limited evaluation of pulmonary parenchyma
No ionizing radiation from MRI component	-

1.5 Spatial Resolution Assessment in PET/CT and PET/MRI

Despite advancements in hybrid imaging technology, enduring challenges remain, especially concerning spatial resolution within PET imaging modalities (Herzog, 2012). In the diagnostic nuclear medicine field of interest, the spatial resolution represents the ability of the system to precisely identify, distinguish and characterize radioactive sources close to each other and it is one of the most crucial parameters for precise diagnosis for healthcare practitioners (Lameka et al., 2016; Townsend, 2008). To analyse the spatial resolution, the calculation of full-width half-maximum (FWHM) is one of the widely used methods (Caribé et al., 2019; NEMA Standards Publication, 2018; U.S. Food and Drug Administration, 2017).

As it is one of the most crucial parameters for a precise diagnosis, constraints in spatial resolution can jeopardize the diagnostic precision of medical imaging. Consequently, substantial attention has been directed towards improving spatial resolution in diagnostic nuclear medicine research. An extensive examination of existing literature reveals numerous studies focused on clarifying, comparing, examining, and enhancing the spatial resolution of various imaging modalities. These investigations cover a broad range of topics, from fundamental principles to practical methodologies, demonstrating a collective effort to address, evaluate, and compare spatial resolution across different imaging platforms like PET/CT and PET/MRI.

Numerous studies have detailly examined the spatial resolution of PET/CT systems, to comprehend their limitations, techniques for spatial resolution determination, and strategies for enhancement. For instance, Surti et al. (2009) conducted a study to investigate the impact of the inter-crystal positioning technique and Compton scatter rejection technique on the spatial resolution of PET systems through Monte Carlo simulations, followed by two whole-body scans. The results showed that near the centre of the scanner, the inter-crystal positioning technique improved spatial resolution by approximately 0.5 mm, whereas the Compton scatter rejection technique yielded higher spatial resolution at the expense of reduced sensitivity. Besides, Lee et al. (2015) conducted a study comparing the impacts of FDG-18 and Zr-89 radiotracers on spatial resolution and image quality in PET/CT imaging utilizing NEMA NU2-2007 standard image quality measurements. Their findings demonstrated that while Zr-89 exhibited inferior spatial resolution compared to

FDG-18, Zr-89 proved effective for immune-PET studies owing to its favourable half-life. Likewise, Braune et al. (2022) explored the efficacy of employing FDG-18, Ga-68-HCl, and Cu-64-HCl radiotracers on image quality using the NEMA PET body phantom, assessing various parameters including spatial resolution, recovery coefficients, coefficient of variation within the background, contrast recovery coefficient, and contrast–noise ratio. Their investigation revealed that the spatial resolution of FDG-18 and Cu-64-HCl was similar, whereas Ga-68-HCl exhibited inferior spatial resolution.

Furthermore, Yoon et al. (2015) proposed iterative algorithms for achieving optimized spatial resolution in PET/CT modalities, employing the NEMA NU 2-2007 standard and a three-point sourced phantom. They recommended the utilization of iterative algorithms such as HD.S, HD, and FBP to enhance image quality in PET/CT modalities. Moreover, Prieto et al. (2010) detailed and validated recovery coefficient-based techniques for assessing spatial resolution in PET scanners. Their work demonstrated that employing recovery coefficients enables the evaluation of tomographic spatial resolution. In addition to these, Su et al. (2023) investigated the impact of various reconstruction techniques on the accuracy and image quality of PET/CT. Their findings indicated that employing ordered subset expectation maximization (OSEM) with point spread function (PSF) modelling led to improved spatial resolution.

Moreover, the combination of OSEM-PSF with OSEM incorporating time-of-flight (TOF) modelling yielded superior results in terms of recovery coefficient mean and contrast recovery coefficient. Additionally, Lodge et al. (2018) assessed the spatial resolution of PET scanners by employing a water-filled oblique-angled cylinder phantom with an FDG-18 radiotracer. Their investigation demonstrated that the recovery coefficients obtained using full-width half maximum closely matched those derived from physical phantoms.

The integration of PET with MRI has heralded new possibilities for hybrid imaging, prompting researchers to investigate the spatial resolution capabilities of PET/MRI systems. Notably, Peng & Levin (2012) conducted a study on spatial resolution and contrast recovery using Monte Carlo simulation and various radiotracers including FDG-18, C-11, N-13, O-15, Ga-68, and Rb-86. They considered factors such as positron diffusion range, collinear photon annihilation, and finite detector element

width. Their findings revealed that increasing the magnetic field up to 10T resulted in comparable outcomes in orthogonal directions for O-15, Ga-68, and Rb-82 compared to FDG-18 without a magnetic field. Similarly, Huang et al. (2014) conducted a study on the impact of uniform magnetic fields (0 T, 3 T, and 7 T) on spatial resolution for high-energy positron emitters such as FDG-18, I-124, and Ga-68 in PET/MRI, utilizing the Geant4 Monte Carlo toolkit submerged in water and suspended in air. Their findings demonstrated that the application of a small uniform magnetic field, such as 3 T, improved spatial resolutions. Additionally, Tian et al. (2022) investigated the effect of the Q.Clear reconstruction method, which is not commonly utilized in PET/MRI modalities, on PET/MRI imaging using FDG-18 and assessed image quality, including spatial resolution, according to the NEMA NU 2-2012 standard. Their study revealed that the Q.Clear method yielded superior spatial resolution compared to OSEM-TOF reconstruction.

1.6 The Purpose of This Thesis

This thesis aims to contribute to existing extensive research into the differentiating capabilities of two important hybrid molecular imaging modalities, PET/CT and PET/MRI. The major goal is to evaluate the spatial resolution quantitatively and qualitatively, and to compare the radioactive source differentiating abilities of PET/CT and PET/MRI using radioactivity against distance graphs generated from image slices acquired with a custom-designed phantom and numerous capillary tubes filled with FDG-18 radiopharmaceutical. Also, this study aims to fill the gap in the distinguishing abilities of medical imaging modalities used in nuclear medicine by directly comparing their distinguishing capabilities (via evaluating peak occurrence characteristics in radioactivity versus distance graphs) and spatial resolution (using full-width half-maximum measurements of each radioactive source in radioactivity versus distance graphs).

In addition, this thesis also aims to provide insight to literature on the spatial resolution measurements using custom-made phantom under the scattering environment as in human body (due to the filled water in the setup) and to compare those results with the ones presented in literature and measured in air environment.

2
MATERIALS AND METHOD

The study was an experimental study that aimed at qualitatively assessing the distinguishing ability and quantitatively determining the spatial resolution of medical imaging modalities employed in nuclear medicine. This was achieved by utilising a custom-designed phantom and FDG-18 radiotracers. The decision to use a custom-designed phantom instead of a well-established technology phantom for spatial resolution assessment of PET imaging systems was made due to its alignment with the study's main objective. Specifically, the study aimed to evaluate the distinguishing ability of PET/CT and PET/MRI against several radioactive sources arranged linearly at varying distances without applying any image processing steps under scattering environment as in the human body.

2.1 Phantom Description

Firstly, the rectangular prism presented in Figure 2.1-A was equipped with two extensions, with dimensions of 20 mm in height, 100 mm in width, and 160 mm in length, and was designed in Solidworks (SOLIDWORKS, n.d.). In two extensions of the prism, suitable elliptical holes were incorporated to facilitate assembly using M4 screws and bolts.

In the mid-line of the prism’s frontal surface, ten cylindrical holes with equal diameters and lengths, which were 3 mm and 80 mm respectively, were drilled to place capillaries filled with radiopharmaceuticals, as shown in Figure 2.1-B.

Secondly, each pair of holes was separated from each other strategically to examine qualitatively the distinguishing ability of imaging modalities, as illustrated in Figure 2.1-B. The first pair separated from each other by 1 mm distance and the separation distance was increased by 1 mm in each following hole until reaching the tenth hole.

Subsequently, two supports with V-shaped profiles with 90-degree presented in Figure 2.1-C, which were designed to fix the prism to the necessary surface of the enclosure made of plexiglass, were designed in Solidworks as well in prism.

Afterwards, two suitable elliptic holes, which matched the ones on extensions of the prism, were drilled to assemble the prism with the supports using M4 screws.

Thirdly, the prism and two supports were manufactured using an additive manufacturing method, 3D printing, from Poly-lactic acid (PLA). PLA was preferred as the raw material because of its enhanced biomimicking properties.

Finally, the phantom was assembled as presented in Figure 2.1-D. To do so, four M4x20 polyamide screws were utilized to firmly fixate the extensions of the prism onto two supports. Polyamide screws were chosen due to MRI compatibility.

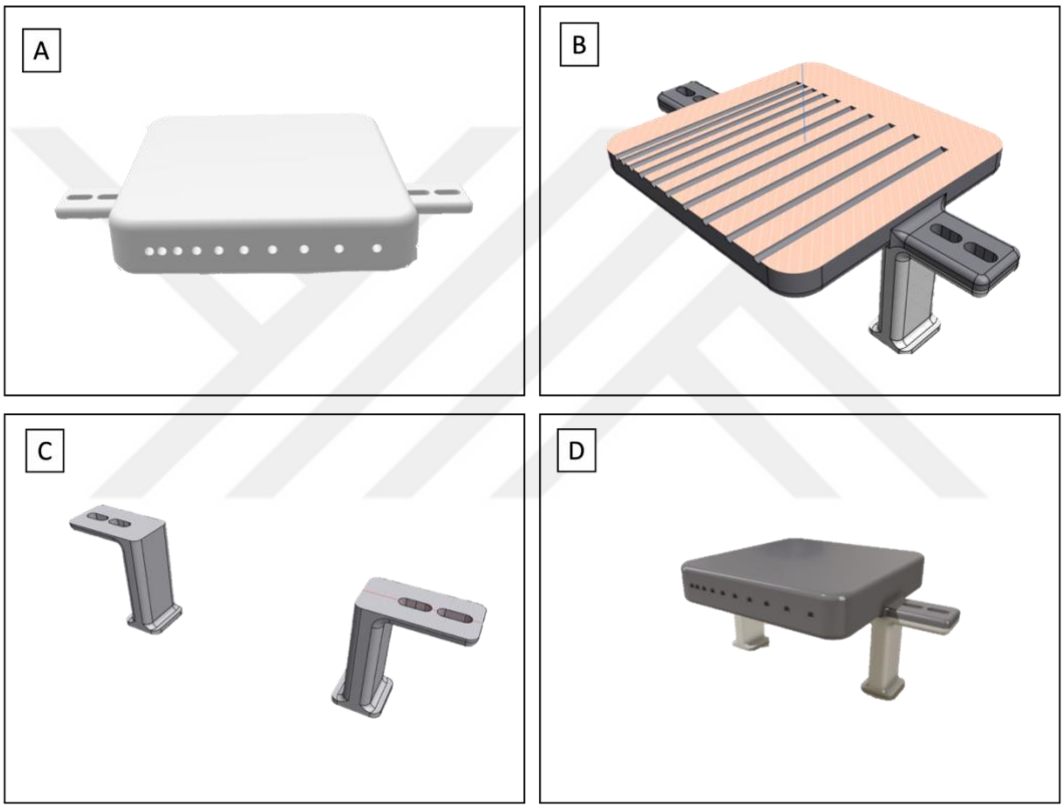


Figure 2.1 The Design Illustration of The Custom-Made PLA Phantom Used in This Thesis. (A) The Design of The Prism with Two Extensions. (B) The Illustration of Holes in The Mid-Section of The Prism's Frontal Surface and Their Strategic Separation. (C) The Design of Two Supports. (D) The Final Assembly of Custom-Made PLA Phantom.

2.2 Experimental Setup

At first, to enclose the 3D-printed custom-made PLA phantom, a plexiglass box was manufactured. It was 200 mm in height, 250 mm in width, 400 mm in length

and 5 mm in thickness to resemble the dimensions of the human thoracoabdominal region. The box was designed, so as to prevent any leakage from the box. To do so, 5 surfaces of the box were glued together with a V-shaped contact profile at 45 degrees and the sixth one, which was the upper surface, was not glued to be used as an access point into the box.

Then, the assembled custom-made phantom was fixed to the left surface of the plexiglass enclosure using a fast adhesive (Akfix, 705), as shown in Figure 2.2. Subsequently, ten microhematocrit tubes (BRIS) were loaded with radiopharmaceutical, which was FDG-18 with a concentration of higher than 200 MBq/cc (5 mCi/cc). To seal the tubes and prevent any radiopharmaceutical contamination inside the phantom and the enclosure, a tube sealing compound (Cha-seal, 510) was used on both ends of the tubes. After that, the tubes were placed the holes in the phantom.

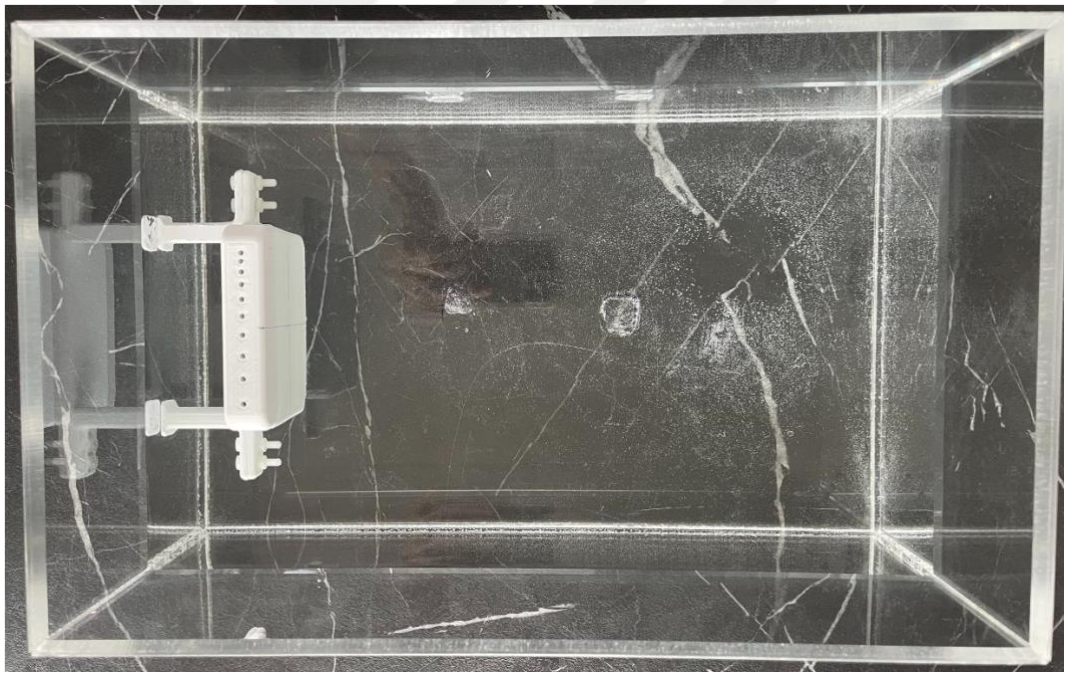


Figure 2.2 The Experimental Setup.

Subsequently, the half of the plexiglass enclosure was filled with water to simulate human body composition and to create scattering environment for measurements as in the human body.

After all these steps, the water-filled experimental setup was placed on the patient bed of imaging modalities, as seen in Figure 2.3 (Picture in PET/MRI cannot be taken, due to safety concerns of the camera and MRI device), PET/CT (Siemens,

Biograph Horizon) and PET/MRI (General Electronics, Signa PET/MRI) respectively.

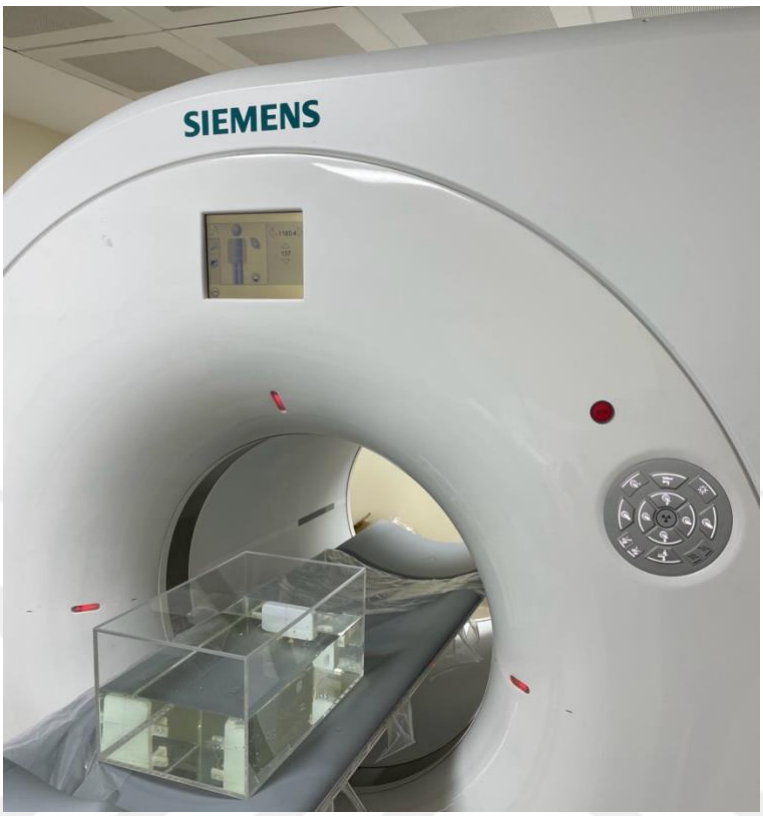


Figure 2.3 Image Acquisition in PET/CT.

Biograph Horizon digital detectors facilitate PET/CT imaging with an impressive volumetric resolution of 78 mm^3, attributed to the small 4x4-mm lutetium oxyorthosilicate (LSO) crystal elements. Additionally, these detectors offer true time-of-flight (TOF) capabilities, enhancing both performance and clinical outcomes. Furthermore, dedicated CT solutions, traditionally exclusive to standalone systems, are now integrated to deliver high-quality imaging at reduced radiation doses (Siemens Healthineers GmbH, 2023).

The SIGNA PET/MR system is engineered to meet the needs of physicians and physicists seeking the extensive potential of time-of-flight (TOF) PET imaging. This system features a lutetium-based scintillator (LBS) with dimensions of 4.0 mm × 5.3 mm × 25 mm and utilizes innovative MR-compatible Silicon Photomultiplier (SiPM) technology, comprising 28 modules, each with 20 blocks per module and 18 anodes per block, totaling 10,080 anodes. SiPM technology addresses the limitations of previous technologies, offering superior TOF timing resolution, high

gain, and low noise characteristic of next-generation photomultipliers. The LBS crystals, with their high light output, rapid timing, and significant stopping power, enable effective TOF PET. These SiPMs are meticulously supported by active and passive thermal compensation, including water cooling. Positioned at the isocenter of the 3.0T magnet, the detectors offer a 25 cm field of view (FOV). The integration of LBS and SiPM technology allows the SIGNA PET/MR to perform TOF PET concurrently with 3.0T MR imaging. The SiPM detector's 25 mm deep crystals and 25 cm FOV enhance sensitivity by three times compared to previous PET technology generations. This detection system also achieves a high Noise Equivalent Count Rate (NECR) for research studies, reaching up to 21 kcps/MBq. Enclosed entirely within the scanner bore, the digital detection system leverages the timing advantages of the SiPM sensor, resulting in exceptional timing resolution that produces images with enhanced contrast and signal-to-noise ratios (General Electronics Healtcare, 2014).

In each device, the phantom in the experimental setup was centred using a laser beam utilized in each device. Followingly, images were taken using the double-bed and single-bed configurations in PET/CT and PET/MRI devices respectively. The images were taken in 4 minutes for each device and the obtained image slices were transferred to the computer.

2.3 Data Analysis

The obtained images from PET/CT and PET/MRI modalities were analysed in Image J (ImageJ, n.d.). It was a medical image analysis tool that is open-sourced, JAVA-based, downloadable and runs on any device with JAVA 1.4 (or higher). In Image J, the clearest PET image slice was determined for each imaging modality.

After that, activity against the distance graph of two selected slices was extracted as datasets in comma-separated values (.csv) format to analyse spatial resolution for both imaging modalities.

Subsequently, each dataset was uploaded to MATLAB (2023b) (MathWorks, 2023) to conduct qualitative and quantitative data analysis of the spatial resolution. For qualitative analysis, MATLAB command lines presented in Appendix A.1 were run. As a result, two activity-against-distance graphs for both imaging modalities

were obtained separately in different figures. Then, activity peaks that occurred in the figures were analysed by comparing them with their original locations and assessing the peak characteristics.

For quantitative analysis, the command lines presented in Appendix A.2 were run. As a result, the FWHM value for each peak in the figures was calculated for both imaging modalities. Then they were compared with the values presented in the literature.

3
RESULTS

3.1 Qualitative Assessment and Comparison

As a result of qualitative analysis of selected image slices, activity vs distance graphs presented in Figure 3.1-B and 3.1-C, were obtained. To compare activity locations detected in image slices, actual radiopharmaceutical-filled tube locations and appeared peak locations were compared as shown in Figure 3.1.

The comparison of activity against the distance graph of PET/CT, Figure 3.1-B and actual radiopharmaceutical location, Figure 3.1-A, revealed that PET/CT could not be able to distinguish the first five sources in phantom and they appeared on the graph as combined peaks. It means that PET/CT could be able to slightly differentiate the radioactive sources after a 5 mm separation distance and clearly differentiate after a 6 mm separation distance.

Furthermore, the comparison of activity against the distance graph of PET/MRI, Figure 3.1-C and actual radiopharmaceutical location, Figure 3.1-A, presented that PET/MRI started to distinguish the sources after the fourth tube in phantom and as in PET/CT undistinguishable sources appeared as combined peaks on the graph. It reveals that PET/MRI is able to slightly distinguish radioactive sources after a 4 mm separation distance and clearly differentiate after a 5 mm separation distance.

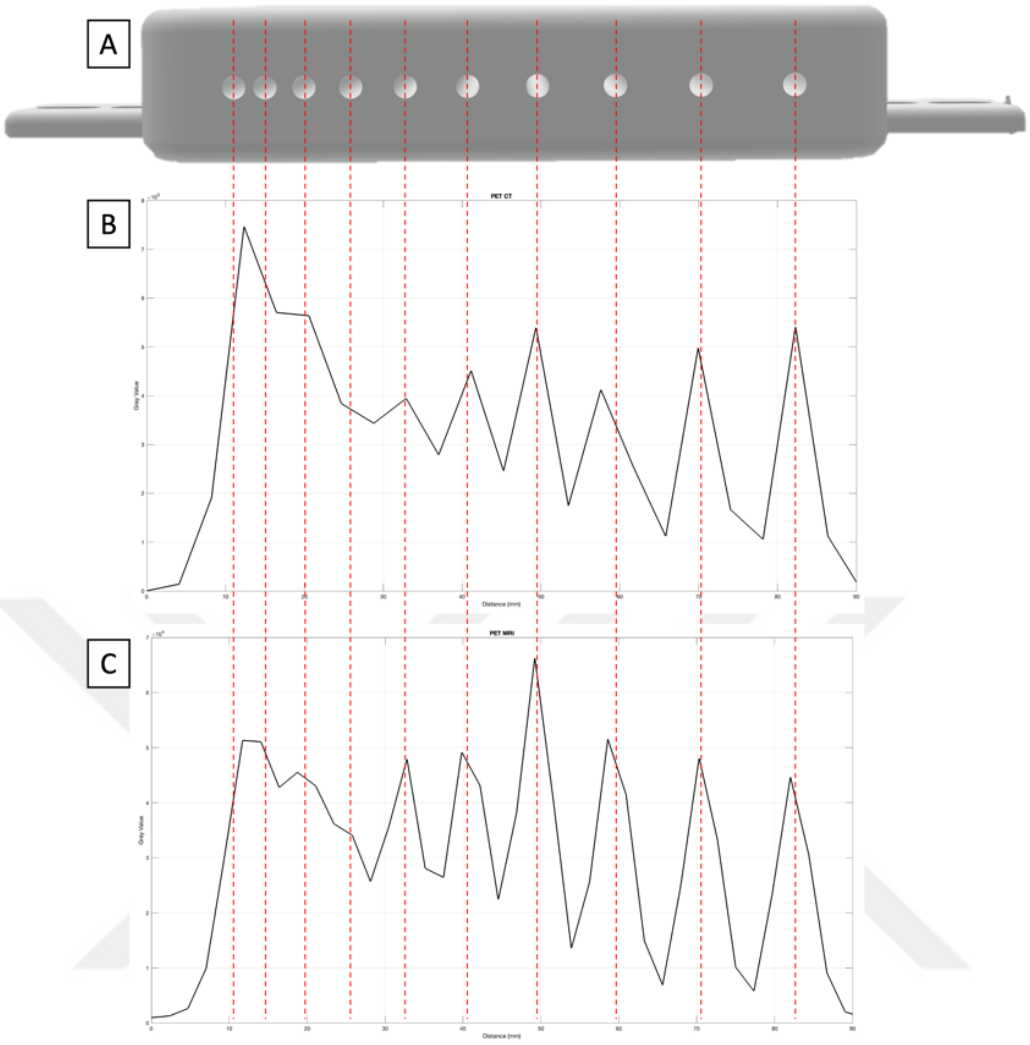


Figure 3.1 The Radioactive Source Positions Loaded on The Phantom and The Corresponding Radioactivity Results. (A) Radioactive Source (FDG-18) Locations onto Phantom. (B) Radioactivity vs Distance (in mm) Graph for PET/CT, (C) Radioactivity vs Distance (in mm) Graph of PET/MRI.

3.2 Quantitative Assessment and Comparison

As a result of the quantitative analysis FWHM values appeared peaks in activity against distance graphs, data presented in Table 3.1 and Table 3.2 for PET/CT and PET/MRI respectively, were obtained.

The FWHM values obtained from peaks that appeared in the PET/CT image slice disclosed that the values belonging to the sources could not be distinguished clearly by PET/CT and could not be calculated due to combined peak characteristics. However, starting from the sources separated by 6 mm from the previous one,

which corresponds seventh and following sources, acceptable FWHM values could be obtained. The calculated FWHM values for PET/CT modality are given in Table 3.1.

Table 3.1 FWHM Results for PET/CT.

Radioactive Source #	FWHM PET/CT (mm)
1	N/A
2	N/A
3	N/A
4	N/A
5	N/A
6	N/A
7	6.87
8	6.21
9	5.76
10	5.18

The FWHM values derived from peaks observed in the PET/MRI image slice indicated that the values, corresponding to the sources were not distinctly distinguishable by PET/MRI, and could not be calculated due to combined peak characteristics. However, after the sources were separated by 5 mm from the previous one, corresponding to the sixth source and beyond, acceptable FWHM values could be obtained. The calculated FWHM values for the PET/MRI system are presented in Table 3.2.

Table 3.2 FWHM results for PET/MRI.

Radioactive Source #	FWHM PET/MRI (mm)
1	N/A
2	N/A
3	N/A
4	N/A
5	N/A
6	N/A
7	6.15
8	6.08
9	5.79
10	5.76

4
DISCUSSION

In this thesis, ten radioactive capillary sources that were spaced apart by varying distances and filled with FDG-18 were loaded into a custom-design phantom, and activity against distance graphs was obtained from image slices of each device to quantitatively and qualitatively determine the spatial resolutions and compare the distinguishing abilities of PET/CT and PET/MRI.

As per the findings of qualitative analysis, PET/CT began to differentiate radioactive sources after the sixth radioactive source, which was five millimetres apart from the previous one and six millimetres from the one after it. However, PET/MRI started to distinguish after the fifth radioactive source, which was separated from the previous one by four millimetres and five millimetres from the one after it. The findings indicate that PET/MRI is superior to PET/CT in its capacity to identify radioactive sources that are located in close proximity. This result validates the literature's existing understanding, which states that PET/MRI performs better in clinical applications than PET/CT in terms of detection (Afaq et al., 2017; Jadvar & Colletti, 2014; Mayerhoefer et al., 2020; Sawicki et al., 2016).

The quantitative analysis results showed that the FWHM values of sources could not be differentiated clearly, yielding unacceptable results due to combined peak characteristics in both PET/CT and PET/MRI. However, the FWHM of well-distinguished radioactive sources (seventh source and subsequent sources, which were separated by six to nine millimetres from the preceding source, respectively) was 6.87 mm, 9.11 mm, 5.76 mm, 5.18 mm for PET/CT and 6.15 mm, 6.08 mm, 5.79 mm, 5.76 mm for PET/MRI from the seventh to tenth source, respectively, while FWHM values in the literature were 5.0 mm, 7.0 mm at 1 cm and 10 cm for PET/CT (U.S. Food and Drug Administration, 2017) and 6.0 mm and 6.9 mm at 1 cm and 10 cm for PET/MRI (Caribé et al., 2019).

As can be seen, the obtained results were slightly different from the existing data in the literature, the reason for the slight variations in FWHM values between our experiment and the literature is that our experiment was conducted underwater to simulate patient body composition, and the goal-oriented specific spacing distances between radioactive sources were smaller than those specified in the NEMA

standard. The literature, on the other hand, used the NEMA NU-2 testing protocol, which requires conducting experiments in the air with fixed spacing distances (1 cm and 10 cm). The variations in FWHM values can explain the variations in scattering patterns of beta particles and the cumulative interference caused by nearby sources.

These results prove how well PET/CT and PET/MRI work as therapeutic tools when several radioactive sources need to be precisely localised, as in the case of biological structures with intricate geometries. A thorough understanding of the restrictions and limits that are specific to each modality can improve imaging technique optimisation and reliable data interpretation. Subsequent studies could investigate methods to improve spatial resolution or sensitivity, which could lead to an improvement in the capacity to distinguish the sources even when they are located closer together. Further insights into the potential and constraints of these imaging modalities may also be obtained by examining the effects of different phantom materials, activity levels, radioactive sources, and image processing techniques on distinguishability.

5
CONCLUSION

This study used FDG-18 radiopharmaceuticals and specially designed phantoms to evaluate spatial resolution qualitatively and quantitatively and to compare the ability to differentiate close activity sources of PET/CT and PET/MRI. The study assessed the features of peak occurrence by examining activity against distance graphs and assessed spatial resolution by using FWHM measurements. The study also underlined how crucial specially designed phantoms are for these kinds of assessments.

As per the outcomes of this thesis, it was discovered that PET/MRI (GE Signa) is more effective than PET/CT (Siemens Biograph Horizon) at differentiating close radioactive sources, which can provide healthcare practitioners with more accurate diagnoses in clinical molecular imaging settings due to its advanced SiPM feature. Additionally, FWHM analysis yielded comparable outcomes with reasonable deviations from the present understanding in the literature.

REFERENCES

Afaq, A., Fraioli, F., Sidhu, H., Wan, S., Punwani, S., Chen, S. H., Akin, O., Linch, D., Ardeshna, K., Lambert, J., Miles, K., Groves, A., & Kayani, I. (2017). Comparison of PET/MRI with PET/CT in the evaluation of disease status in lymphoma. *Clinical Nuclear Medicine*, *42*(1), e1. https://doi.org/10.1097/RLU.0000000000001344

Ahmed, S. N. (2007). *Physics and Engineering of Radiation Detection* (First). Academic Press Inc. https://books.google.com.tr/books?hl=tr&lr=&id=3KdmdcGbBywC&oi=fnd&pg=PP1&dq=Physics+%26+Engineering+of+Radiation+Detection&ots=J1mCIHr5hs&sig=IX6I8U182ZZeioFC1zS-d5iFQtw&redir_esc=y#v=onepage&q=Physics%20%26%20Engineering%20of%20Radiation%20Detection&f=false

Ariño, G., Chmeissani, M., De Lorenzo, G., Puigdengoles, C., Cabruja, E., Calderón, Y., Kolstein, M., Macias-Montero, J. G., Martinez, R., Mikhaylova, E., & Uzun, D. (2013). *Energy and coincidence time resolution measurements of CdTe detectors for PET*. https://doi.org/10.1088/1748-0221/8/02/C02015

Bailey, D. L., & Townsend, D. W. (2005). *Positron Emission Tomography: Basic Sciences* (P. E. Valk & M. N. Maisey, Eds.; 1st ed.). Springer.

Barry, N. P. E., & Sadler, P. J. (2013). Exploration of the medical periodic table: towards new targets †. *Chem. Commun*, *49*, 5106. https://doi.org/10.1039/c3cc41143e

Basic Physics of Nuclear Medicine/Interaction of Radiation with Matter - Wikibooks, open books for an open world. (n.d.). Retrieved March 24, 2024, from https://en.wikibooks.org/wiki/Basic_Physics_of_Nuclear_Medicine/Interaction_of_Radiation_with_Matter

Becquerel, A. H. (1896). Sur les radiations invisibles émises par les sels d'uranium. *CR Acad. Sci. Paris*, *122*, 420.

Becquerel, A. H. (1903). *On radioactivity, a new property of matter* (A. H. Becquerel, Ed.). Les prix Nobel.

Braune, A., Oehme, L., Freudenberg, R., Hofheinz, F., Van Den Hoff, J., Kotzerke, J., & Hoberück, S. (2022). Comparison of image quality and spatial resolution between 18 F, 68 Ga, and 64 Cu phantom measurements using a digital Biograph Vision PET/CT. *EJNMMI Physics*, *9*, 58. https://doi.org/10.1186/s40658-022-00487-7

Bryan, J. C. (2023). *Introduction to Nuclear Science - Jeff C. Bryan - Google Kitaplar*. https://books.google.com.tr/books?hl=tr&lr=&id=lxi8EAAAQBAJ&oi=fnd&pg=PP1&dq=Bryan,+J.+C.+(2023).+Introduction+to+Nuclear+Science.+CRC+Press.&ots=CNUJyZ48yp&sig=yo4j1LDd1j5JEjqI7sZGo8QkBZc&redir_esc=y#v=onepage&q&f=false

Bushberg, J. T. (2012). *The essential physics of medical imaging*. Wolters Kluwer Health/Lippincott Williams & Wilkins.

Caribé, P. R. R. V., Koole, M., D'Asseler, Y., Deller, T. W., Van Laere, K., & Vandenberghe, S. (2019). NEMA NU 2–2007 performance characteristics of GE Signa integrated PET/MR for different PET isotopes. *EJNMMI Physics*, *6*(1), 1–13. https://doi.org/10.1186/S40658-019-0247-X/FIGURES/3

Chandra, R., & Rahmin, A. (2018). *Nuclear Medicine Physics: The Basics* (S. Zinner & A. Ferran, Eds.; Eight edition).

Cheetham, P. J., & Petrylak, D. P. (2012). Alpha Particles as Radiopharmaceuticals in the Treatment of Bone Metastases: Mechanism of Action of Radium-223 Chloride (Alpharadin) and Radiation Protection. *Monmouth Junction*, *26*(4), 330–340.

Crișan, G., Moldovean-cioroianu, N. S., Timaru, D. G., Andrieș, G., Căinap, C., & Chiș, V. (2022). Radiopharmaceuticals for PET and SPECT Imaging: A Literature Review over the Last Decade. In *International Journal of Molecular Sciences* (Vol. 23, Issue 9). MDPI. https://doi.org/10.3390/ijms23095023

Das, A., & Ferbel, T. (2003). Introduction to Nuclear and Particle Physics. In *Introduction to Nuclear and Particle Physics* (Second). WORLD SCIENTIFIC. https://doi.org/10.1142/5460

Dash, A., Knapp, F. F., & Pillai, M. (2014). Targeted Radionuclide Therapy - An Overview. *Current Radiopharmaceuticals*, *6*(3), 152–180. https://doi.org/10.2174/1874471013066660023

De Vincentis, G., Gerritsen, W., Gschwend, J. E., Hacker, M., Lewington, V., O'Sullivan, J. M., Oya, M., Pacilio, M., Parker, C., Shore, N., & Sartor, O. (2019). Advances in targeted alpha therapy for prostate cancer. In *Annals of Oncology* (Vol. 30, Issue 11, pp. 1728–1739). Elsevier Ltd. https://doi.org/10.1093/annonc/mdz270

Ehman, E. C., Johnson, G. B., Villanueva-Meyer, J. E., Cha, S., Leynes, A. P., Larson, P. E. Z., & Hope, T. A. (2017). PET/MRI: Where might it replace PET/CT? *Journal of Magnetic Resonance Imaging*, *46*(5), 1247–1262. https://doi.org/10.1002/JMRI.25711

Ersahin, D., Doddamane, I., & Cheng, D. (2011). Targeted radionuclide therapy. In *Cancers* (Vol. 3, Issue 4, pp. 3838–3855). https://doi.org/10.3390/cancers3043838

FORRER, F., WALDHERR, C., MAECKE, H. R., & MUELLER-BRAND, J. (2006). Targeted Radionuclide Therapy with 90Y-DOTATOC in Patients with Neuroendocrine Tumors. *ANTICANCER RESEARCH*, *26*, 703–708.

General Electronics Healtcare. (2014). *SIGNA ™ PET/MR Technical Data*. SIGNA ™ PET/MR Technical Data.

Gibbons, T. (2019). *Radioactivity — Definition & Overview - Expii*. https://www.expii.com/t/radioactivity-definition-overview-8744

Greene, R. E., Pressly, R. S., & Case, F. N. (1972). *A Review of Alpha Radiation Source Preperation Methods and Applications*. https://www.osti.gov/servlets/purl/4624732

Herzog, H. (2012). PET/MRI: Challenges, solutions and perspectives. *Zeitschrift Für Medizinische Physik*, *22*(4), 281–298. https://doi.org/10.1016/J.ZEMEDI.2012.07.003

Hoefnagel, C. A. (1991). European Journal of Nuclear Medicine Radionuclide therapy revisited. In *Eur J Nucl Med* (Vol. 18).

HOEFNAGEL, C. A. (1998). Radionuclide cancer therapy. *Annals of Nuclear Medicine*, *12*(2), 61–70.

Huang, S. Y., Savic, D., Yang, J., Shrestha, U., & Seo, Y. (2014). The Effect of Magnetic Field on Positron Range and Spatial Resolution in an Integrated Whole-Body Time-Of-Flight PET/MRI System. *IEEE Nuclear Science Symposium Conference Record. Nuclear Science Symposium*, *2014*. https://doi.org/10.1109/NSSMIC.2014.7431006

ImageJ. (n.d.). *ImageJ*. ImageJ. Retrieved April 29, 2024, from https://imagej.net/ij/index.html

Itali, V., Erin, V., Ouri, Y., Opowski, P., Olfgang, W., Auerwein, S., Arkus, M., Ins, L., Yörgy, G., Ovacs, K., Artyn, M., Homas, T., Rancis, F., Alman, C., Lemens, C., Isco, D., & Erruys, A. W. S. (2001). The New England Journal of Medicine ENDOLUMINAL BETA-RADIATION THERAPY FOR THE PREVENTION OF CORONARY RESTENOSIS AFTER BALLOON ANGIOPLASTY A BSTRACT Background Beta radiation is effective in reducing. In *N Engl J Med* (Vol. 344, Issue 4). www.nejm.org

Jadvar, H., & Colletti, P. M. (2014). Competitive advantage of PET/MRI. *European Journal of Radiology*, *83*(1), 84–94. https://doi.org/10.1016/j.ejrad.2013.05.028

Kang, H. G., & Yamaya, T. (2021). Multi Imaging Devices: PET/MRI. *Handbook of Particle Detection and Imaging: Second Edition*, 1317–1357. https://doi.org/10.1007/978-3-319-93785-4_51

Kassis, A. I., & Adelstein, S. J. (2005). *Radiobiologic Principles in Radionuclide Therapy*.

Khalil, M. M. (2011). *Basic Sciences of Nuclear Medicine* (Vol. 1).

King III, S. B., Williams, D. O., Chougule, P., Larry Klein, J., Waksman, R., Hilstead, R., Macdonald, J., Anderberg, K., & Crocker, I. R. (1998). *Endovascular-Radiation to Reduce Restenosis After Coronary Balloon*

Angioplasty Results of the Beta Energy Restenosis Trial (BERT). http://ahajournals.org

Kirwan, J. F., Rennie, C., & Evans, J. R. (2009). Beta radiation for glaucoma surgery. In *Cochrane Database of Systematic Reviews* (Issue 2). John Wiley and Sons Ltd. https://doi.org/10.1002/14651858.CD003433.pub2

Kocher, D. C. (1981). *A Handbook of Decay Data for Application to Radiation Dosimetry and Radiological Assessments*.

Lameka, K., Farwell, M. D., & Ichise, M. (2016). Positron Emission Tomography. *Handbook of Clinical Neurology*, *135*, 209–227. https://doi.org/10.1016/B978-0-444-53485-9.00011-8

Lancaster, J. L., & Hasegawa, B. H. (2017). *Fundamental mathematics and physics of medical imaging*.

L'Annunziata, M. F. (2012). *Handbook of Radioactivity Analysis - Google Kitaplar* (M. F. L'Annunziata, Ed.; 3rd ed., Vol. 1). Elsevier. https://books.google.com.tr/books?hl=tr&lr=&id=S4FrejzJy0cC&oi=fnd&pg=PP1&dq=L%E2%80%99Annunziata,+M.+F.+(2012).+Handbook+of+Radioactivity+Analysis.+Academic+Press.&ots=25s2WQ1lom&sig=ASoVHrYQTcnY6UKqLR-8eugegOY&redir_esc=y#v=snippet&q=%22radioactive%20decay%22&f=false

Lee, Y. S., Kim, J. S., Kim, J. Y., Kim, B. Il, Lim, S. M., & Kim, H. J. (2015). Spatial Resolution and Image Qualities of Zr-89 on Siemens Biograph TruePoint PET/CT. *Cancer Biotherapy & Radiopharmaceuticals*, *30*(1), 27. https://doi.org/10.1089/CBR.2014.1709

Leroy, C., & Rancoita, P.-G. (2009). *Principles of Radiation Interaction in Matter and Detection* (Second edition).

Levitt, A. B., Robinson, K., Wellons, E., Lai, K. M., Cui, J. H., Gannon, B., & Rosenthal, D. (2004). Prevention of intimal hyperplasia: Initial results with low-dose beta-radiation applied by an external vascular polymer wrap. *Cardiovascular Radiation Medicine*, *5*(1), 34–37. https://doi.org/10.1016/j.carrad.2004.03.002

Lodge, M. A., Leal, J. P., Rahmim, A., Sunderland, J. J., & Frey, E. C. (2018). Measuring PET Spatial Resolution Using a Cylinder Phantom Positioned at an Oblique Angle. *J Nucl Med*, *59*, 1768–1775. https://doi.org/10.2967/jnumed.118.209593

Martin, C., & Godes, R. (2018). *Confinement Induced Electron Capture*.

MathWorks. (2023). *MathWorks - Makers of MATLAB and Simulink - MATLAB & Simulink*. MathWorks. https://www.mathworks.com/?s_tid=mlh_gn_logo

Mayerhoefer, M. E., Prosch, H., Beer, L., Tamandl, D., Beyer, T., Hoeller, C., Berzaczy, D., Raderer, M., Preusser, M., Hochmair, M., Kiesewetter, B., Scheuba, C., Ba-Ssalamah, A., Karanikas, G., Kesselbacher, J., Prager, G., Dieckmann, K., Polterauer, S., Weber, M., … Haug, A. R. (2020). PET/MRI versus PET/CT in oncology: a prospective single-center study of 330 examinations focusing on implications for patient management and cost considerations. *European Journal of Nuclear Medicine and Molecular Imaging*, *47*(1), 51–60. https://doi.org/10.1007/S00259-019-04452-Y/TABLES/3

Melcher, C. L. (2000). Scintillation Crystals for PET. *Journal of Nuclear Medicine*, *41*, 1051–1055. http://www.snm.org

Milano, F., Lewis, C., Sprawls, P., Tabakov, S., & Strand, S.-E. (2013). Encyclopaedia of MEDICAL PHYSICS. In *Encyclopaedia of MEDICAL PHYSICS: Vol. Volume I and II* (pp. 3–63).

Morgenstern, A., Apostolidis, C., & Bruchertseifer, F. (2020). Supply and Clinical Application of Actinium-225 and Bismuth-213. In *Seminars in Nuclear Medicine* (Vol. 50, Issue 2, pp. 119–123). W.B. Saunders. https://doi.org/10.1053/j.semnuclmed.2020.02.003

Murshed, H. (2019). Fundamentals of Radiation Oncology: Physical, Biological, and Clinical Aspects - Google Kitaplar. In *Fundamentals of Radiation Oncology: Physical, Biological, and Clinical Aspects* (Third Edition, Vol. 1, pp. 6–9). https://books.google.com.tr/books?hl=tr&lr=&id=UpqCDwAAQBAJ&oi=fnd&pg=PP1&dq=Fundamentals+of+Radiation+Oncology+Physical

,+Biological,+and+Clinical+Aspects&ots=KuukS0JPFX&sig=LyHC3_1D5LMj-4deFeFOxdowlXU&redir_esc=y#v=onepage&q=Fundamentals%20of%20Radiation%20Oncology%20Physical%2C%20Biological%2C%20and%20Clinical%20Aspects&f=false

Najam, H., Dearborn, M. C., & Tafti, D. (2023). Nuclear Medicine Instrumentation. *StatPearls*. https://www.ncbi.nlm.nih.gov/books/NBK597384/

NAKABEPU, Y., & NAKAJO, M. (1994). Radionuclide therapy of malignant pheochromocytoma with 131I-MIBG. *Annals of Nuclear Medicine*, *8*(4), 259–268.

NEMA Standards Publication. (2018). NU 2-2018 Performance Measurements of Positron Emission Tomographs (PETS). In *National Electrical Manufacturers Association*. www.nema.org

Pajic, B., & Greiner, R. H. (2005). Long term results of non-surgical, exclusive strontium-/yttrium-90 beta-irradiation of pterygia. *Radiotherapy and Oncology*, *74*(1), 25–29. https://doi.org/10.1016/j.radonc.2004.08.022

Parker, C., Heidenreich, A., Nilsson, S., & Shore, N. (2018). Current approaches to incorporation of radium-223 in clinical practice. In *Prostate Cancer and Prostatic Diseases* (Vol. 21, Issue 1, pp. 37–47). Nature Publishing Group. https://doi.org/10.1038/s41391-017-0020-y

Parker, C., Lewington, V., Shore, N., Kratochwil, C., Levy, M., Lindén, O., Noordzij, W., Park, J., & Saad, F. (2018). Targeted Alpha Therapy, an Emerging Class of Cancer Agents: A Review. In *JAMA Oncology* (Vol. 4, Issue 12, pp. 1765–1772). American Medical Association. https://doi.org/10.1001/jamaoncol.2018.4044

Peng, H., & Levin, C. S. (2012). Study of PET intrinsic spatial resolution and contrast recovery improvement for PET/MRI systems. *Physics in Medicine & Biology*, *57*, N101. https://doi.org/10.1088/0031-9155/57/9/N101

Popovtzer, A., Rosenfeld, E., Ben-Hur, R., Mizrachy, A., Kelson, I., & Keisari, Y. (2018). A New Radiation Concept, Treatment of Squamous Cell Carcinoma by Alpha-radiation Based Brachytherapy (Alpha DaRT). *International Journal of Radiation Oncology*Biology*Physics*, *102*(3), e275. https://doi.org/10.1016/j.ijrobp.2018.07.886

Powsner, R. A., Palmer, M. R., & Powsner, EdwardR. (2013). *Essentials of Nuclear Medicine Physics and Instrumentation* (Vol. 1).

Powsner, R. A., & Powsner, E. R. (2006). *Essential Nuclear Medicine Physics* (M. Sugden & L. Brindley, Eds.; Second). Blackwell Publishing. https://books.google.com.tr/books?hl=tr&lr=&id=8jswRw_UMnsC&oi=fnd&pg=PR5&dq=essential+nuclear+medicine+physics+second+edition&ots=xpNoECLm4V&sig=YlI1n9LVQHTCu9lw3MYAIuSRodU&redir_esc=y#v=onepage&q=essential%20nuclear%20medicine%20physics%20second%20edition&f=false

Prieto, E., Martí-Climent, J. M., Arbizu, J., Garrastachu, P., Domínguez, I., Quincoces, G., García -Velloso, M. J., Lecumberri, P., Gómez-Fernández, M., & Richter, J. A. (2010). Evaluation of Spatial Resolution of a PET scanner through the simulation and experimental measurement of the Recovery Coefficient. *Computers in Biology and Medicine*, *40*(1), 75–80.

Qaim, S. M. (2001). Therapeutic radionuclides and nuclear data. In *Radiochim. Acta* (Vol. 89).

Qiao, C. K., Wei, J. W., & Chen, L. (2021). An overview of the compton scattering calculation. In *Crystals* (Vol. 11, Issue 5). MDPI AG. https://doi.org/10.3390/cryst11050525

Radiation Basics | NRC.gov. (2020, March 20). https://www.nrc.gov/about-nrc/radiation/health-effects/radiation-basics.html

Rahman, M. O. (2017). *DOSE DISTRIBUTION TO THE DIFFERENT ORGANS FOR VARIOUS FIELD SIZE(S) USING ALDERSON RANDO PHANTOM FOR 60CO GAMMA BEAM DURING RADIOTHERAPY PROCEDURE* [BANGLADESH UNIVERSITY OF ENGINEERING & TECHNOLOGY]. https://www.researchgate.net/publication/285374859

Razibul Hasan, M., Harunor Rashid Khan, M., Rashedur Rahman, M., Shohel Parvez, M., Rakibul Islam, M., & Kumar Paul, A. (2017). Quality Control of Gamma Camera with SPECT Systems. *Clinical Engineering and Radiation Oncology*, *6*, 225–232. https://doi.org/10.4236/ijmpcero.2017.63021

Roth, D., Larsson, E., Ljungberg, M., & Sjögreen Gleisner, K. (2022). Monte Carlo modelling of a compact CZT-based gamma camera with application to 177Lu imaging. *EJNMMI Physics*, *9*(1), 1–21. https://doi.org/10.1186/S40658-022-00463-1/FIGURES/7

Rutherford, E., & Royds, T. (1899). XXI. The nature of the α-particle from radioactive substances. *The London, Edinburgh, and Dublin Philosophical Magazine and Journal of Science*, *17*(98), 281–286.

Saturnino Guarino, D., & Martelli, F. (2018). *Mathematical Modelling, Numerical and Data Analysis BIOCHEMISTRY AND TECHNOLOGY OF [18 F]FLUTEMETAMOL FOR THE AMYLOID PET IMAGING IN ALZHEIMER'S DISEASE*. www.universitas-studiorum.it

Sauter, A. W., Wehrl, H. F., Kolb, A., Judenhofer, M. S., & Pichler, B. J. (2010). Combined PET/MRI: one step further in multimodality imaging. *Trends in Molecular Medicine*, *16*(11), 508–515. https://doi.org/10.1016/j.molmed.2010.08.003

Sawicki, L. M., Grueneisen, J., Buchbender, C., Schaarschmidt, B. M., Gomez, B., Ruhlmann, V., Wetter, A., Umutlu, L., Antoch, G., & Heusch, P. (2016). Comparative Performance of 18 F-FDG PET/MRI and 18 F-FDG PET/CT in Detection and Characterization of Pulmonary Lesions in 121 Oncologic Patients. *J Nucl Med*, *57*, 582–586. https://doi.org/10.2967/jnumed.115.167486

Serruys, P. W., Sianos, G., Van der Giessen, W., Bonnier, H. J. R. M., Urban, P., Wijns, W., Benit, E., Vandormael, M., Dörr, R., Disco, C., Debbas, N., & Silber, S. (2002). Intracoronary β-radiation to reduce restenosis after balloon angioplasty and stenting: The Beta Radiation in Europe (BRIE) study. *European Heart Journal*, *23*(17), 1351–1359. https://doi.org/10.1053/euhj.2001.3153

Sgouros, G., Bodei, L., McDevitt, M. R., & Nedrow, J. R. (2020). Radiopharmaceutical therapy in cancer: clinical advances and challenges. In *Nature Reviews Drug Discovery* (Vol. 19, Issue 9, pp. 589–608). Nature Research. https://doi.org/10.1038/s41573-020-0073-9

Shaffer, T. M., Drain, C. M., & Grimm, J. (2016). Optical imaging of ionizing radiation from clinical sources. In *Journal of Nuclear Medicine* (Vol. 57, Issue 11, pp. 1661–1666). Society of Nuclear Medicine Inc. https://doi.org/10.2967/jnumed.116.178624

Shukla, A. K., & Kumar, U. (2006). Positron emission tomography: An overview. In *Journal of Medical Physics* (Vol. 31, Issue 1). http://journals.lww.com/jomp

Siemens Healthineers GmbH. (2023). *Siemens Biograph Horizon Brochure*. Siemens, Biograph Horizon Brochure.

SOLIDWORKS. (n.d.). *SOLIDWORKS | 3D CAD Design Software & PDM Systems*. SOLIDWORKS. Retrieved April 29, 2024, from https://www.solidworks.com/

Sóti, Z., Magill, J., & Dreher, R. (2019). Karlsruhe Nuclide Chart – New 10th edition 2018 . *EPJ Nuclear Sciences & Technologies*, *5*, 6. https://doi.org/10.1051/epjn/2019004

Su, X., Geng, J., Liu, J., Liu, F., Wu, Y., Zheng, R., & Wang, X. (2023). Influence of reconstruction techniques on PET/CT image quality and quantitative accuracy: a phantom study. *Radiation Detection Technology and Methods*, 1–16. https://doi.org/10.1007/S41605-023-00441-W/METRICS

Surti, S., Scheuermann, R., Werner, M. E., & Karp, J. S. (2009). Improved spatial resolution in PET scanners using sampling techniques. *IEEE Transactions on Nuclear Science*, *56*(3), 596. https://doi.org/10.1109/TNS.2009.2013389

Tian, D., Yang, H., Li, Y., Cui, B., & Lu, J. (2022). The effect of Q.Clear reconstruction on quantification and spatial resolution of 18F-FDG PET

in simultaneous PET/MR. *EJNMMI Physics*, *9*(1), 1–12. https://doi.org/10.1186/S40658-021-00428-W/FIGURES/4

Townsend, D. W. (2008). *Positron Emission Tomography/Computed Tomography*. https://doi.org/10.1053/j.semnuclmed.2008.01.003

Townsend, D. W., & Cherry, S. R. (2001). Combining anatomy and function: The path to true image fusion. *European Radiology*, *11*(10), 1968–1974. https://doi.org/10.1007/S003300101007/METRICS

Troutner, D. E. (1987). Chemical and physical properties of radionuclides. *International Journal of Radiation Applications and Instrumentation. Part B. Nuclear Medicine and Biology*, *14*(3), 171–176. https://doi.org/10.1016/0883-2897(87)90039-0

Tsai, Y. J., & Liu, C. (2021). Pitfalls on PET/CT due to artifacts and instrumentation. *Seminars in Nuclear Medicine*, *51*(6), 646. https://doi.org/10.1053/J.SEMNUCLMED.2021.06.015

Types of Radiation [MOE]. (n.d.). Retrieved May 1, 2024, from https://www.env.go.jp/en/chemi/rhm/basic-info/2018/01-03-02.html

U.S. Food and Drug Administration. (2017). Premarket Notification (510(k)) for K162736. In *U.S. Food and Drug Administration*.

Wadsak, W., & Mitterhauser, M. (2010). Basics and principles of radiopharmaceuticals for PET/CT. In *European Journal of Radiology* (Vol. 73, Issue 3, pp. 461–469). https://doi.org/10.1016/j.ejrad.2009.12.022

Washington, C. M., & Leaver, D. (2015). Principles and Practice of Radiation Therapy. In C. M. Washington & D. Leaver (Eds.), *Principles and Practice of Radiation Therapy* (Fourth, Vol. 1, pp. 270–293). Elsevier.

Welsh, J. S. (2006). Beta Radiation. *The Oncologist*, *11*(2), 181–183. https://doi.org/10.1634/theoncologist.11-2-181

Yeong, C. H., Cheng, M. hua, & Ng, K. H. (2014). Therapeutic radionuclides in nuclear medicine: Current and future prospects. In *Journal of Zhejiang University: Science B* (Vol. 15, Issue 10, pp. 845–863). Zhejiang University Press. https://doi.org/10.1631/jzus.B1400131

Yoon, H. J., Jeong, Y. J., Son, H. J., Kang, D.-Y., Hyun, K.-Y., & Lee, M.-K. (2015). Optimization of the spatial resolution for the GE discovery PET/CT 710 by using NEMA NU 2-2007 standards. *Article in Journal of the Korean Physical Society*, *66*(2), 287–294. https://doi.org/10.3938/jkps.66.287

Zamanian, A., & Hardiman, C. (2005). *Electromagnetic Radiation and Human Health: A Review of Sources and Effects*.

Zanzonico, P. (2004). *Positron Emission Tomography: A Review of Basic Principles, Scanner Design and Performance, and Current Systems*. https://doi.org/10.1053/j.semnuclmed.2003.12.002

Zimmermann, R., & Pouchot, P. (2019). *Nuclear medicine : radioactivity for diagnosis and therapy*. EDP Sciences.

A
APPENDIX MATERIALS AND METHOD

Appendix A.1

```
clear all; close all; clc;

%%
% Read data from CSV file
data_petCT = csvread('PET_CT_Activity_vs_Location_data_slice215.csv');
data_petMRI = csvread('PET_MRI_Activity_vs_Location_data_slice678.csv');

x_1 = data_petCT(:, 1);
y_1 = data_petCT(:, 2);

x_2 = data_petMRI(:, 1);
y_2 = data_petMRI(:, 2);

% Generate new x values
distance_petCT = linspace(0, 90, 2500);
distance_petMRI = linspace(0, 90, 2500);

% Linear interpolation
grayValue_petCT = interp1(x_1, y_1, distance_petCT, 'linear');
grayValue_petMRI = interp1(x_2, y_2, distance_petMRI, 'linear');

%% Plottings for PET CT and PET MRI
% PET CT
figure();
plot(distance_petCT, grayValue_petCT);
title("PET CT");
xlabel("Distance (mm)");
ylabel("Gray Value");
grid on;

% PET MRI
figure();
plot(distance_petMRI, grayValue_petMRI);
title("PET MRI")
xlabel("Distance (mm)");
ylabel("Gray Value");
grid on;
```

Appendix A.2

```
clear all; close all; clc;

%%
% Read data from CSV file
data_petCT = csvread('PET_CT_Activity_vs_Location_data_slice215.csv');
data_petMRI = csvread('PET_MRI_Activity_vs_Location_data_slice678.csv');

x_1 = data_petCT(:, 1);
y_1 = data_petCT(:, 2);

x_2 = data_petMRI(:, 1);
y_2 = data_petMRI(:, 2);

% Generate new x values
distance_petCT = linspace(0, 90, 2500);
distance_petMRI = linspace(0, 90, 2500);

% Linear interpolation
grayValue_petCT = interp1(x_1, y_1, distance_petCT, 'linear');
grayValue_petMRI = interp1(x_2, y_2, distance_petMRI, 'linear');

%% FWHM calculation and plotting for PET CT

% Finds peaks and their locations
   [peaks_CT, locs_CT] = findpeaks(grayValue_petCT);

   % Initialize FWHM and FWTM arrays
   fwhm_values_CT = zeros(size(peaks_CT));

   % Loops through each peak
   for i = 1:length(peaks_CT)
      % Finds the peak position and maximum value
      peakValue = peaks_CT(i);
      peakIndex = find(grayValue_petCT == peakValue);

      % Finds the half-maximum value
      halfMax_CT = peakValue / 2;

      % Finds the points where the signal crosses half-maximum value
      halfLeftIndex = find(grayValue_petCT(1:peakIndex) <= halfMax_CT, 1, 'last');
      halfRightIndex = peakIndex + find(grayValue_petCT(peakIndex:end) <=
halfMax_CT, 1, 'first')-1;

      % Calculates FWHM
      fwhm_values_CT(i) = distance_petCT(halfRightIndex) -
distance_petCT(halfLeftIndex);
      % fwhm_values_CT(i) = (distance_petCT(halfRightIndex) -
distance_petCT(halfLeftIndex)) / 1.2;

      % Displays FWHM for each peak
      disp(['FWHM of PET CT peak #', num2str(i), ': ', num2str(fwhm_values_CT(i))]);
      disp(' ');
      disp(' ');

      % Plots the result for each peak
      figure;
      plot(distance_petCT, grayValue_petCT, 'k-', 'LineWidth', 2);
      hold on;
```

```
        plot(distance_petCT(peakIndex), peakValue, 'go', 'LineWidth', 2);
        plot([distance_petCT(halfLeftIndex), distance_petCT(halfRightIndex)],
[halfMax_CT, halfMax_CT], 'r--', 'LineWidth', 2);
        title(['PET CT ', 'Peak #', num2str(i), ', FWHM Calculation']);
        xlabel('Distance (mm)');
        ylabel('Gray Value');
        legend('Signal', 'Peak', 'Half-Maximum');
        grid on;
    end

    %% FWHM calculation and plotting for PET MRI
% Finds peaks and their locations
    [peaks_MRI, locs_MRI] = findpeaks(grayValue_petMRI);

    % Initialize FWHM and FWTM arrays
    fwhm_values_MRI = zeros(size(peaks_MRI));

    % Loops through each peak
    for i = 1:length(peaks_MRI)
        % Finds the peak position and maximum value
        peakValue = peaks_MRI(i);
        peakIndex = find(grayValue_petMRI == peakValue);

        % Finds the half-maximum value
        halfMax_MRI = peakValue / 2;

        % Finds the points where the signal crosses half-maximum value
        halfLeftIndex = find(grayValue_petMRI(1:peakIndex) <= halfMax_MRI, 1, 'last');
        halfRightIndex = peakIndex + find(grayValue_petMRI(peakIndex:end) <=
halfMax_MRI, 1, 'first') - 1;

        % Calculates FWHM
        fwhm_values_MRI(i) = distance_petMRI(halfRightIndex) -
distance_petMRI(halfLeftIndex);
        % fwhm_values_MRI(i) = (distance_petMRI(halfRightIndex) -
distance_petMRI(halfLeftIndex)) / 1.2;
        % Displays FWHM for each peak
        disp(['FWHM of PET MRI peak #', num2str(i), ': ', num2str(fwhm_values_MRI(i))]);
        disp(' ');
        disp(' ');
        % Plots the result for each peak
        figure;
        plot(distance_petMRI, grayValue_petMRI, 'k-', 'LineWidth', 2);
        hold on;
        plot(distance_petMRI(peakIndex), peakValue, 'go', 'LineWidth', 2);
        plot([distance_petMRI(halfLeftIndex), distance_petMRI(halfRightIndex)],
[halfMax_MRI, halfMax_MRI], 'r--', 'LineWidth', 2);
        title(['PET MRI ', 'Peak #', num2str(i), ', FWHM Calculation']);
        xlabel('Distance (mm)');
        ylabel('Gray Value');
        legend('Signal', 'Peak', 'Half-Maximum');
        grid on;
    end
```

PUBLICATIONS FROM THE THESIS

Conference Papers

1. Paper 1: 5th International Conference on Natural and Applied Science and Engineering (ICNASEN-2024), Title: Assessment of Spatial Resolution in PET/CT, Theme: 5, Abstract No: 4, Presentation Type: Oral